

# Evolution of UV–NIR structural properties of cluster galaxies<sup>★,★★</sup>

F. La Barbera<sup>1</sup>, G. Busarello<sup>1</sup>, M. Massarotti<sup>1</sup>, P. Merluzzi<sup>1</sup>, and A. Mercurio<sup>2</sup>

<sup>1</sup> INAF, Istituto Nazionale di Astrofisica Osservatorio Astronomico di Capodimonte, via Moiariello 16, 80131 Napoli, Italy  
e-mail: labarber@na.astro.it

<sup>2</sup> Università degli Studi di Trieste, Department of Astronomy, Trieste, Italy

Received 25 November 2002 / Accepted 19 May 2003

**Abstract.** We study the structure and the internal colour gradients of cluster galaxies from UV to NIR restframe, in the redshift range  $z = 0.21$ – $0.64$ . Structural parameters (half light radius  $r_e$ , mean surface brightness  $\langle\mu\rangle_e$  and Sersic index  $n$ ) are derived for galaxies in the clusters A 209 at  $z = 0.21$  and EIS 0048 at  $z = 0.64$ . This data set, together with previous data for the cluster AC 118 at  $z = 0.31$ , constitutes the first large ( $N \sim 270$ ) sample of cluster galaxies whose internal structure in UV, optical (OPT) and NIR ( $U$ -,  $V$ - and  $H$ -band restframe) can be investigated up to a look-back time of  $\sim 6$  Gyr ( $\Omega_m = 0.3$ ,  $\Omega_\Lambda = 0.7$  and  $H_0 = 70 \text{ km s}^{-1} \text{ Mpc}^{-1}$ ). Galaxies are classified as spheroids or disks according to the shape of the light profile, and the evolution of the two populations are investigated separately. On average, both spheroids and disks are more concentrated at longer wavelengths: the galaxy sizes become smaller from UV to NIR, while Sersic indices increase. This trend shows an evolution in disks, where the mean ratio of optical to NIR Sersic indices decreases from  $z = 0.31$  to  $z = 0.64$ . Colour gradients are on average negative at all redshifts and are stronger in disks than in spheroids. But while for spheroids both grad (UV–OPT) and grad (OPT–NIR) are only weakly dependent on redshift, the optical–NIR gradients of disks become significantly smaller at  $z = 0.64$ . Colour gradients and central colours are compared with models of metallicity, age, and dust extinction gradients. Metallicity turns out to be the primary driver of colour gradients in spheroids, the age gradient being constrained to be smaller than  $\sim 25\%$ . For disks, two kinds of models fit the present data: (i) age gradients (in the range [30, 50]%) with significant dust extinction, and (ii) “pure” dust models, in which the gradients of colour excess are a factor of two higher in EIS 0048 than in the other clusters. Since colour gradients of disks seem not to correlate significantly with inclination, we argue that age gradient models could represent a more likely explanation of the present data, in agreement with what expected on the basis of hierarchical merging scenarios.

**Key words.** galaxies: clusters: individual: A 209, AC 118, EIS 0048 – galaxies: photometry – galaxies: evolution – galaxies: fundamental parameters (*colours, colour gradients, effective radii, Sersic indices*)

## 1. Introduction

Studies of spectral indices and broadband colours have demonstrated that stellar populations in galaxies are not homogeneous, but are characterized by a spatial variation in their physical properties.

Most of nearby early-type (E) galaxies have negative colour gradients, becoming bluer toward the periphery (e.g. Boroson et al. 1983; Franx et al. 1989; Peletier et al. 1990a, 1990b, hereafter PDI90 and PVJ90, respectively; Michard 1999). The presence of radial changes in colour may be interpreted in terms of both age and metallicity, due to the well known degeneracy between the two properties (Worthey et al. 1996). The most effective way to investigate the origins of colour gradients is

to study their evolution with look-back time, since age and metallicity models give very different predictions at increasing redshifts (Kodama & Arimoto 1997). By adopting this approach, Saglia et al. (2000) and Tamura & Ohta (2000) analyzed the colour profile of Es in distant clusters by using HST optical photometry. They found that galaxies show moderate colour gradients also at intermediate redshifts, and claimed, therefore, that metallicity is the primary factor driving the observed gradients. The same conclusion was drawn by Tamura et al. (2000) and by Hinkley & Im (2001) for early-type galaxies in the field. On the other hand, there are also some indications that the population of spheroids at intermediate redshifts is not homogeneous with respect to the radial properties of the stellar populations. Recently, Bartholomew et al. (2001) showed that cluster K+A galaxies at intermediate redshifts could have somewhat bluer colour gradients with respect to normal early-types, while Menanteau et al. (2001) found positive colour gradients for spheroids in the Hubble Deep Fields, concluding that a significant fraction of galaxies have experienced recent star formation localized in the center.

Send offprint requests to: P. Merluzzi,  
e-mail: merluzzi@na.astro.it

\* Based on observations collected at European Southern Observatory (ESO ObsID. 62.0–0369, 63.0–0257, 64.0–0236, 67.A–0044, 67.B–0044, 68.A–0116.

\*\* Figures of Appendix C are only available in electronic form at <http://www.edpsciences.org>

Various attempts have been made to interpret the existence of colour gradients of early-type galaxies in the framework of different evolutionary models. The presence of metallicity gradients is naturally expected within the monolithic collapse scenarios (Larson 1974), as a consequence of the later onset of the galactic wind in the inner region of the galaxy, but it can also be accommodated within the framework of galaxy formation via hierarchical merging (White 1980; Mihos & Hernquist 1994). Positive colour gradients are not predicted by the monolithic collapse while they can be explained as a consequence of the centrally peaked star formation produced in merging remnants (Mihos & Hernquist 1994, 1996). Recently, it has been shown that colour gradients of spheroids can also be explained within the chemodynamical model for evolution of elliptical galaxies (see Friaca & Terlevich 2001 and references therein).

The origin of colour gradients is crucial to understand the mechanisms underlying the formation and evolution of late-type galaxies. Colour gradients in nearby disks have been extensively investigated by de Jong (1996) using optical and near-infrared broadband photometry. He found that disk galaxies have more metal rich and older stellar populations in the center, and that, therefore, both age and metallicity drive the observed radial colour profiles. The presence of age gradients is also supported by the increase of the disk scale-lengths measured by the  $H_\alpha$  flux with respect to the optical (Ryder & Dopita 1994). Further investigations have been performed by Gadotti & dos Anjos (2001), who studied a large sample of late-type spirals in the field by UV–optical photometry. They found that most of the galaxies (85%) have negative or null colour gradients, and suggested that colour gradients are more sensitive to age than to metallicity of stellar populations. Disks in the cluster environment have been studied with NIR ( $J - K$ ) data by Moriondo et al. (2001), who found very weak or null colour gradients.

The presence of age gradients is a robust prediction of hierarchical models, in which spiral bulges contain older stars than their associated disks, which form by subsequent accretion. Evidence in favour of the presence of age gradients for field spirals at intermediate redshifts has been found by Abraham et al. (1999).

A crucial role in the interpretation of colour gradients can be played by dust absorption. Although the effects of extinction remain still unclear and substantially unresolved (e.g. Tamura et al. 2000; de Jong 1996; Gadotti & dos Anjos 2001), different studies have shown that dust absorption could have an important effect in the internal colour distributions of galaxies (e.g. Wise & Silva 1996; Silva & Elston 1994). In particular, for what concerns disk dominated galaxies, it has been proved that internal extinction strongly affects the colour profile of late-type spirals (e.g. Peletier et al. 1995). For these reasons, in the present work we consider simple extinction gradient models for disk galaxies.

An effective tool to analyze the internal light distribution in galaxies is the comparison of structural parameters (like the half light radius and the Sersic index) at different wavelengths. This approach allows large samples of galaxies to be studied with a broad photometric coverage. By using ground-based data, La Barbera et al. (2002, hereafter LBM02) obtained the first large sample ( $N = 94$ ) of both optical and NIR

structural parameters for cluster galaxies at  $z \sim 0.3$ . They suggested that both age and metallicity could drive the observed colour gradients in the cluster populations. In the present work, we re-analyze this subject by using a larger sample ( $N \sim 270$ ) of cluster galaxies at different redshifts ( $z = 0.21, 0.31, 0.64$ ) with a broader photometric baseline: from UV to NIR restframe. We estimate colour gradients for both disks and spheroids, with the aim of following the properties of both cluster populations down to  $z = 0.64$ .

The layout of the paper is the following. In Sect. 2 we describe the samples used for the present analysis. The derivation of structural parameters is outlined in Sect. 3, while Sect. 4 deals with the comparison of UV–NIR parameters at the different redshifts. The distributions of colour gradients are analyzed in Sect. 5, and their evolution with redshift is compared with predictions of metallicity, age, and extinction models in Sect. 6. Summary and conclusions are drawn in Sect. 7. In the following, we will assume the cosmology  $\Omega_m = 0.3$ ,  $\Omega_\Lambda = 0.7$  and  $H_0 = 70 \text{ km s}^{-1} \text{ Mpc}^{-1}$ . With these parameters, the age of the universe is  $\sim 13.5$  Gyr, and the redshifts  $z = 0.21$ ,  $z = 0.31$  and  $z = 0.64$  correspond to look-back times of  $\sim 2.5, 3.5$  and  $6$  Gyr, respectively.

## 2. The data

The data relevant for the present study have been collected at the ESO New Technology Telescope and at the ESO Very Large Telescope. They include images in  $B$  and  $R$  bands for the cluster A 209 at  $z = 0.21$  (RA<sub>2000</sub> = 01:31:57.5, Dec<sub>2000</sub> = -13:34:35), in  $R$  and  $K$  bands for the cluster AC 118 at  $z = 0.31$  (RA<sub>2000</sub> = 00:14:19.5, Dec<sub>2000</sub> = -30:23:19), and in  $V$ ,  $I$  (high resolution, HR) and  $K$  bands for the cluster EIS 0048 at  $z = 0.64$  (RA<sub>2000</sub> = 00:48:31.6, Dec<sub>2000</sub> = -29:43:18.0). A 209 and AC 118 are rich, massive clusters of galaxies, with velocity dispersions of  $1394 \pm 94 \text{ km s}^{-1}$  (Mercurio et al. 2003a, hereafter MGB03) and  $1950 \pm 334 \text{ km s}^{-1}$  (Wu et al. 1999), respectively, and with high X-ray luminosity ( $L_X \sim 13.8 \times 10^{44} \text{ erg s}^{-1}$ , see Ebeling et al. 1996, and  $L_X = 62.44 \pm 14.41 \times 10^{44} \text{ ergs s}^{-1}$ , see Wu et al. 1999, respectively). Their velocity field and spatial structure suggest the presence of substructures, with a complex dynamical scenario (see MGB03 and Andreon 2001, respectively). EIS 0048 is a cluster of galaxies having a velocity dispersion of  $\sim 720 \text{ km s}^{-1}$  (Lobo et al. 2002), which is typical for clusters at the same redshift, and a spatial structure which shows evident signs of substructures (see La Barbera et al. 2003). A ROSAT PSPC image, which serendipitously contains the cluster field, indicates the presence of X-ray emission.

The reduction of the photometric data of A 209 and AC 118, and that of the  $V$ - and  $K$ -band images for EIS 0048 is described in Mercurio et al. (2003b, MMM03), Busarello et al. (2002) and Andreon (2001), and La Barbera et al. (2003, hereafter LMI03), respectively. The reduction of the  $I$ (HR)-band image for EIS 0048 is described in Appendix A. Structural parameters have been derived for galaxies of AC 118 in LBM02<sup>1</sup>,

<sup>1</sup> With respect to LBM02, we excluded two galaxies whose light profiles turned out to be strongly affected by nearby objects.

**Table 1.** Relevant information on the samples. Column 1: cluster identification. Column 2: redshift. Column 3: wavebands. Column 4: instruments used for the observation. Column 5: pixel scale relative to each waveband in arcsec/pixel. Column 6: *FWHM* (arcsec) of the seeing for each waveband. Column 7: number of spheroids. Column 8: number of disks. For EIS 0048 two values are reported, since the sample with *K*-band data covers a smaller area. Column 9: completeness magnitudes. Column 10: selection used to assign cluster membership,  $z_p$  and  $z_s$  denote photometric and spectroscopic redshifts, respectively. Column 11: references for details on data reduction and on the definition of cluster membership. The following abbreviations are used: Mercurio et al. (2003a, MGB03), Mercurio et al. (2003b, MMM03), Busarello et al. (2002, BML02), Andreon (2001, A01), La Barbera et al. (2003, LMI03). Note that one out of the  $N = 20$  disks with OPT and NIR data in EIS 0048 does not have UV structural parameters, and therefore the total number of disks at  $z = 0.64$  is 38.

CLUSTER (1)	$z$ (2)	Wavebands (3)	Instr. (4)	Scale (5)	Seeing (6)	$N_{\text{SPH}}$ (7)	$N_{\text{D}}$ (8)	$M_c$ (9)	Sel. (10)	Ref. (11)
A 209	0.21	<i>B, R</i>	EMMI	0.27, 0.27	0.8, 0.9	64	26	$R = 20$	$z_s$	MGB03, MMM03
AC 118	0.31	<i>R, K</i>	EMMI, SOFI	0.27, 0.29	1.0, 0.8	76	15	$R = 21$	$z_p$	BML02, A01
EIS 0048	0.64	<i>V, I, K</i>	FORS2, ISAAC	0.2, 0.1, 0.15	0.6, 0.35, 0.45	54, 32	37, 20	$I = 22$	$z_p$	LMI03

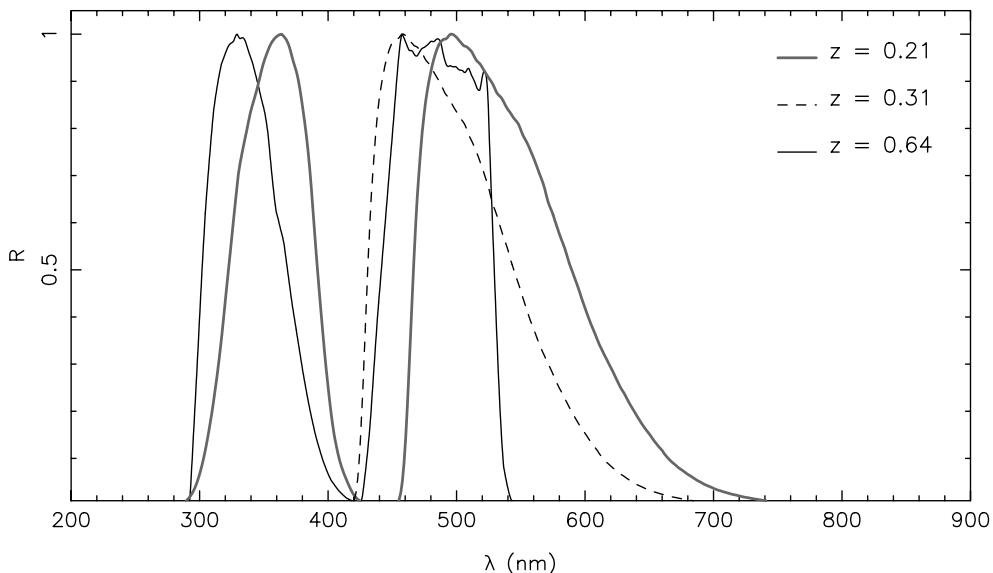


**Fig. 1.** Restframe filter response of the optical photometric wavebands for A 209, AC 118, and EIS 0048. The curves are normalized to 1 at the maximum and are drawn by different types of lines as shown in the upper-right.

while the surface photometry for A 209 and EIS 0048 is presented in the next section. The relevant information on the samples are summarized in Table 1.

In Fig. 1, we show the response curves of the optical filters in the restframe for each cluster. We see that the *R* band for A 209 and AC 118, and the *I* band for EIS 0048 cover approximately the same restframe spectral interval, with a central wavelength ranging between  $\sim 4800$  Å and  $\sim 5200$  Å. These wavebands are close to the *V*-band restframe and will be indicated in the following as optical (OPT) wavebands. The *B* filter at  $z = 0.21$  and the *V* filter at  $z = 0.64$  have central wavelengths in the range 3200–3600 Å, and correspond therefore to *U* restframe. In the following, they will be indicated as UV wavebands. For what concerns the *K* band (hereafter NIR), it covers approximately *H* and *J* restframe at  $z = 0.31$  and at  $z = 0.64$ , respectively. We note that colour gradients and variations in the structural parameters between *J* and *K* bands are expected to be very small (see Silva & Elston 1994) and therefore the

differences of the restframe corresponding to the *K* bands at  $z = 0.31$  and  $z = 0.64$  are negligible for the present analysis. The data of A 209 and AC 118 allow UV–OPT and OPT–NIR properties of cluster galaxies at  $0.2 < z < 0.3$  to be studied, while the same wavelength range is covered at  $z = 0.64$  by *V*, *I* and *K* bands. Since *K* corrections do not affect differences in colour, the UV–OPT and OPT–NIR colour gradients correspond closely to *U*–*V* and *V*–*H* gradients restframe. We point out that the present samples constitute the first large data set of cluster galaxies with structural parameters measured from UV to NIR at intermediate redshifts.

For each cluster we study separately the properties of disks and spheroids. The separation between the two classes is performed on the basis of the Sersic index  $n$  in the optical, since the optical parameters are common to each cluster sample. We define as spheroids the objects with  $n > 2$ , and as disks the remaining galaxies. Following van Dokkum et al. (1998), this criterion corresponds to distinguishing objects with a low

bulge fraction (<20%) from galaxies with a more prominent bulge component. We note that the mean value<sup>2</sup> of  $n$  for disks is  $1.10 \pm 0.06$ . By using numerical simulations, we estimated that this value describes galaxies with a very low bulge fraction ( $L_B/L_{TOT} \sim 0.07$ ). Therefore, although central bulges can affect the properties of some disks, their effect on the bulk properties of disks can be neglected. We also note that, taking into account luminosity distances and K+E corrections, the completeness magnitudes in Table 1 correspond approximately to the same absolute magnitude limits<sup>3</sup>:  $M_V = -19.70 \pm 0.06$  at  $z = 0.21$ ,  $M_V = -19.7 \pm 0.1$  at  $z = 0.31$ , and  $M_V \sim -20.0 \pm 0.2$  at  $z = 0.64$ . K and evolution corrections were obtained by the GISSSEL00 synthesis code (Bruzual & Charlot 1993), with spectral models having an exponential star formation rate, and the uncertainties on  $M_V$  were estimated by computing E corrections for different models, exploring a wide range of stellar population parameters (i.e. metallicity, formation epoch, time scale of star formation).

### 3. Derivation of structural parameters

Structural parameters were derived for A 209 and EIS 0048 by following the procedure described in LBM02. We give here only a brief outline of the method, while details can be found in that paper.

Galaxy images are fitted by the convolution of an accurate model of the Point Spread Function (PSF) with a model of the galaxy light distribution. In this work, we consider Sersic models:

$$I(r) = I_0 \cdot \exp\left(-b \cdot (r/r_e)^{1/n}\right), \quad (1)$$

where  $r$  is the equivalent radius,  $r_e$  is the effective radius,  $I_0$  is the central surface brightness,  $n$  is the Sersic index, and  $b$  is a constant ( $b \sim 2n - 1/3$ , see Caon et al. 1993). The fits were performed by constructing an interactive mask for each galaxy, and by modelling simultaneously overlapping objects. The PSFs were modelled by a multi-Gaussian expansion, taking into account possible variations with the chip position. With respect to LBM02, we had also to consider that the PSF of the FORS2  $I$ -band images showed significant deviations from the circular shape. Details can be found in Appendix B, where we illustrate the PSF modelling for the  $I$ -band images of EIS 0048. The fitted surface brightness profiles are shown in Appendix C.

For AC 118, the typical uncertainties on the structural parameters were estimated in LBM02 by comparing the ground-based parameters with measurements obtained by HST data. The quoted uncertainties amount to  $\sim 38\%$  in  $r_e$  and  $\sim 20\%$  in  $n$ .

<sup>2</sup> The mean value is computed for AC 118 and EIS 0048 galaxies, for which we obtained  $\bar{n} = 1.2 \pm 0.1$  and  $\bar{n} = 1.0 \pm 0.05$ , respectively. For A 209 we found a higher value,  $\bar{n} = 1.5 \pm 0.1$ , due to the presence of a larger fraction of galaxies with  $n \rightarrow 2$ . We found, however, that considering as disks only the galaxies with  $n < 1.3$  in A 209 does not change the estimates (e.g. mean colour gradients) given throughout the paper.

<sup>3</sup> Colour gradients of nearby galaxies seem not to correlate with luminosity (see PDI90), and, therefore, slightly different magnitude limits should not affect studies of colour gradients.

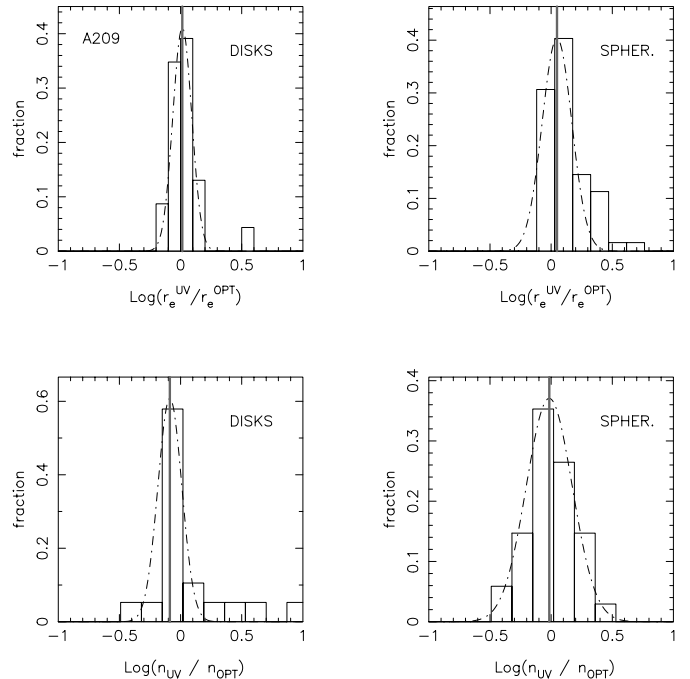


**Fig. 2.** Comparison of UV and optical structural parameters of spheroids (left panels) and disks (right panels) for the cluster A 209. Upper and lower panels refer to the effective radii and Sersic indices, respectively. The vertical grey line marks the mean of the Gaussian fit (dot-dashed line) to the distribution.

For A 209, the errors on  $r_e$  and  $n$  were estimated by using numerical simulations. We found  $\delta r_e \sim 20\%$  and  $\delta n \sim 13\%$ . For EIS 0048, due to the very good quality of the images, the uncertainties on  $r_e$  and  $n$  turned out to be smaller. By comparing measurements obtained for galaxies in common between different pointings, we obtained  $\delta r_e/r_e \sim 15\%$  and  $\delta n/n \sim 10\%$ . The estimates of  $\delta r_e$  and  $\delta n$  were used to derive the uncertainties on the colour gradients (see Sect. 5).

### 4. Structure of galaxies from UV to NIR

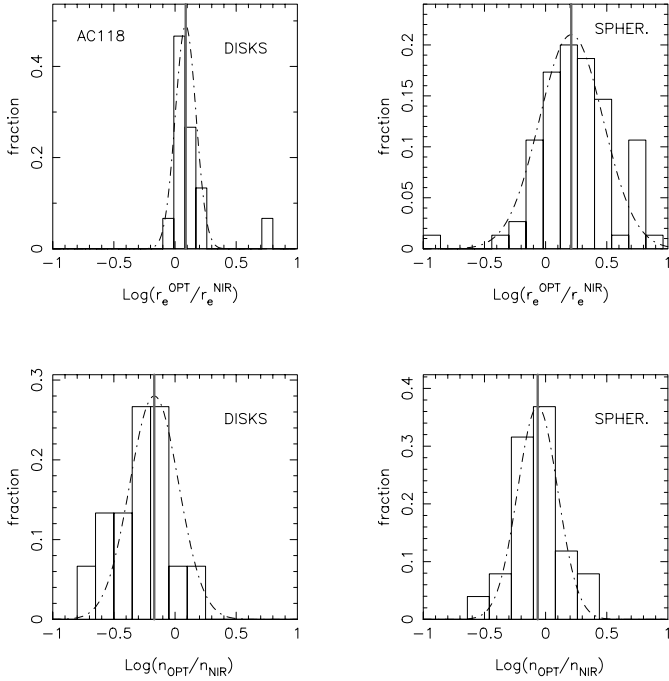
The shape of the light profile for the Sersic models can be fully characterized in terms of the effective radius and the Sersic index. The differences of  $r_e$  and  $n$  between the various wavebands are shown in Figs. 2–5. Differences are always computed between shorter and longer wavelengths. Figures 2 and 4 show the UV–OPT comparison for A 209 and EIS 0048, respectively, while Figs. 3 and 5 show the OPT–NIR parameters for AC 118 and EIS 0048, respectively. In each figure, left and right panels refer to disks and spheroids, while upper and lower panels refer to  $r_e$  and  $n$ , respectively. In order to analyze the overall properties of each distribution, we derived the corresponding mean value and standard deviation by applying the bi-weight statistics (e.g. Beers et al. 1990), that has the advantage to minimize the effect of outliers in the distributions. The values and the corresponding uncertainties, obtained by the bootstrap method, are shown in Tables 2 and 3 for disks and spheroids, respectively.

**Table 2.** Comparison of structural parameters of disks.

$z$	UV–OPT				OPT–NIR			
	$\Delta(\log r_e)$		$\Delta(\log n)$		$\Delta(\log r_e)$		$\Delta(\log n)$	
	mean	std	mean	std	mean	std	mean	std
0.21	$0.01 \pm 0.04$	$0.08 \pm 0.02$	$-0.09 \pm 0.02$	$0.10 \pm 0.04$	...	...	...	...
0.31	...	...	...	...	$0.09 \pm 0.02$	$0.10 \pm 0.02$	$-0.17 \pm 0.04$	$0.20 \pm 0.05$
0.64	$0.045 \pm 0.016$	$0.09 \pm 0.02$	$-0.06 \pm 0.03$	$0.15 \pm 0.02$	$0.10 \pm 0.02$	$0.13 \pm 0.07$	$-0.34 \pm 0.05$	$0.25 \pm 0.06$

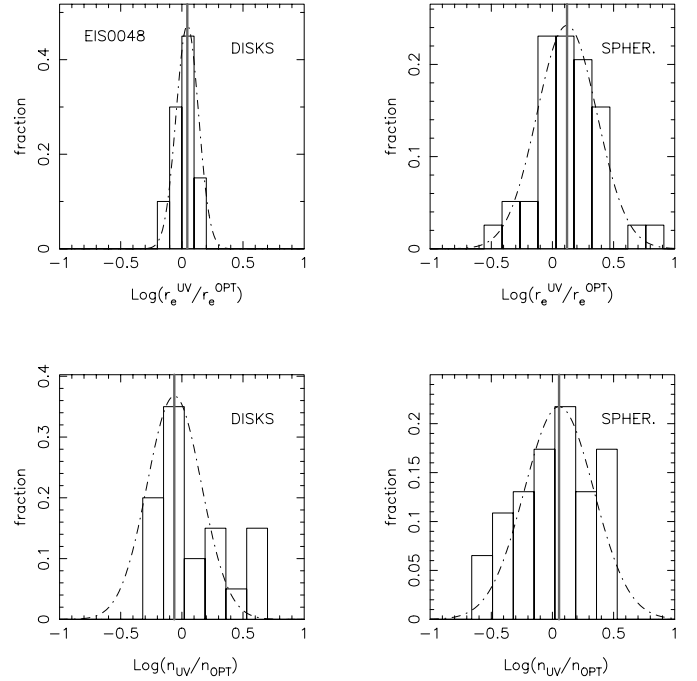
**Table 3.** Comparison of structural parameters of spheroids.

$z$	UV–OPT				OPT–NIR			
	$\Delta(\log r_e)$		$\Delta(\log n)$		$\Delta(\log r_e)$		$\Delta(\log n)$	
	mean	std	mean	std	mean	std	mean	std
0.21	$0.050 \pm 0.025$	$0.12 \pm 0.02$	$-0.02 \pm 0.07$	$0.19 \pm 0.03$	...	...	...	...
0.31	...	...	...	...	$0.21 \pm 0.05$	$0.26 \pm 0.04$	$-0.03 \pm 0.02$	$0.14 \pm 0.04$
0.64	$0.12 \pm 0.03$	$0.24 \pm 0.03$	$0.05 \pm 0.06$	$0.28 \pm 0.04$	$0.080 \pm 0.015$	$0.14 \pm 0.04$	$-0.19 \pm 0.05$	$0.20 \pm 0.20$


**Fig. 3.** The same of Fig. 2 for optical and NIR structural parameters of galaxies in AC 118.

#### 4.1. Disks

By looking at Table 2, we see that disk galaxies tend to have more flat and extended profiles in the UV than in the optical. We find, in fact,  $n^{\text{UV}} < n^{\text{OPT}}$  and  $r_e^{\text{UV}} > r_e^{\text{OPT}}$  both for A 209 and for EIS 0048, although the mean value of  $\Delta(\log r_e)$  at  $z = 0.21$  is not significantly different from zero within the corresponding uncertainty. The mean value of  $n^{\text{UV}}/n^{\text{OPT}}$  is  $\sim 0.8$  at  $z = 0.21$  and  $\sim 0.87$  at  $z = 0.64$ , while the value of  $r_e^{\text{UV}}/r_e^{\text{OPT}}$  ranges from  $\sim 1.02$  for A 209 to  $\sim 1.11$  for EIS 0048. We note that these difference are within  $1\sigma$  and, therefore, are not very significant. At  $z = 0.64$ , disks have larger dispersion in the


**Fig. 4.** Same of Fig. 2 for the cluster EIS 0048.

$\log(n^{\text{UV}}/n^{\text{OPT}})$  diagram, with a standard deviation that is  $\sim 3/2$  of that at  $z = 0.21$ . The effect is clearly seen by comparing Figs. 2 and 4, and is particularly significant in view of the fact that the uncertainties on the structural parameters of EIS 0048 are smaller with respect to those of AC 118 and A 209.

Disk galaxies in AC 118 and EIS 0048 have, on average,  $r_e^{\text{OPT}} > r_e^{\text{NIR}}$  and  $n^{\text{OPT}} < n^{\text{NIR}}$  (see Table 2), and show, therefore, the same trend observed in the UV–OPT comparison: at larger wavelengths, the light profile becomes more concentrated. On average, the value of  $r_e^{\text{OPT}}/r_e^{\text{NIR}}$  is  $\sim 1.23$  at  $z = 0.21$  and  $\sim 1.26$  at  $z = 0.64$ , and  $n^{\text{OPT}}/n^{\text{NIR}}$  decreases from  $\sim 0.7$  to  $\sim 0.45$ . While the behaviour of  $r_e^{\text{OPT}}/r_e^{\text{NIR}}$  is similar to that found in the

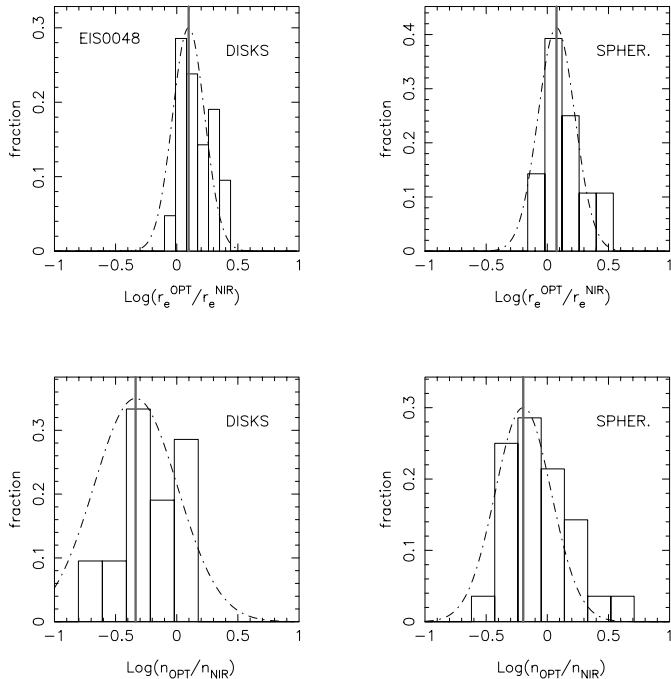


**Fig. 5.** Same of Fig. 3 for the cluster EIS 0048.

UV–OPT, we see that the value of  $n^{\text{OPT}}/n^{\text{NIR}}$  shows a much larger variation, with a strong decrease for EIS 0048. We will further investigate this point in the analysis of colour gradients (Sect. 5.1.1). It is also interesting to note that the distribution of  $\Delta \log(n)$  at  $z = 0.31$  has a significant tail toward negative values, showing that also for AC 118 there are some disks whose NIR light is very peaked in the center with respect to the optical.

Finally, we point out that, since galaxies of AC 118 and EIS 0048 are selected by the photometric redshift technique, we cannot exclude that the previous results can be affected by the contamination of the cluster samples at  $z = 0.64$  by field galaxies, whose properties, also at low redshift, are known to be more disperse and heterogeneous with respect to those of galaxies in the cluster environment. The role of field contamination will be further addressed in Sect. 5.1.1, in the comparison of colour gradients.

#### 4.2. Spheroids

By comparing UV and optical parameters we see that, on average, spheroids have  $r_e^{\text{UV}} > r_e^{\text{OPT}}$ . The mean value of  $r_e^{\text{UV}}/r_e^{\text{OPT}}$  is  $\sim 1.12$  at  $z = 0.21$  and  $\sim 1.32$  at  $z = 0.64$ , while  $n^{\text{UV}}/n^{\text{OPT}}$  is consistent with zero at both redshifts within the corresponding uncertainty. These results indicate that the value of  $r_e^{\text{UV}}/r_e^{\text{OPT}}$  could increase slightly with  $z$  while possible variations of  $n^{\text{UV}}/n^{\text{OPT}}$  are too small to be significant. It is also interesting to note that the dispersions of the two distributions are remarkably larger at  $z = 0.64$ , ranging from  $\sim 0.12$  to  $\sim 0.24$  for  $\log r_e$  and from  $\sim 0.19$  to  $\sim 0.28$  for  $\log n$ . This is similar to what found for the disks and implies that the structural properties of cluster galaxies become more heterogeneous at  $z = 0.64$ . Since a low fraction of spheroids at  $z = 0.64$  are expected to be field

galaxies ( $\sim 10$ – $15\%$ , see Sect. 8.1 of LMI03), these results should not to be affected by field contamination.

For what concerns the OPT–NIR parameters, we find that, on average,  $r_e^{\text{OPT}} > r_e^{\text{NIR}}$  and  $n^{\text{OPT}} < n^{\text{NIR}}$  for both AC 118 and EIS 0048. The mean value of  $n^{\text{OPT}}/n^{\text{NIR}}$  varies from  $\sim 0.93$  at  $z = 0.31$  to  $\sim 0.65$  at  $z = 0.64$ , while  $r_e^{\text{OPT}}/r_e^{\text{NIR}}$  seems to be larger at  $z = 0.31$ , ranging from  $\sim 1.20$  for EIS 0048 to  $\sim 1.6$  for AC 118. This trend is opposite to that found for disks and for spheroids in the UV–OPT. As it is evident from the large dispersion of the distribution in Fig. 3 (upper–right panel), this effect could be not real but due to the uncertainties on the estimated structural parameters at  $z \sim 0.3$ . We note, in fact, that also the standard deviation of the  $\log(r_e^{\text{OPT}}/r_e^{\text{NIR}})$  distribution shows a different trend with  $z$  with respect to that found for the disks and for the spheroids in the UV–OPT: it seems to decrease from  $z \sim 0.31$  to  $z \sim 0.64$ . More NIR data at  $z < 0.6$  would be needed in order to further investigate the previous trends.

## 5. Colour gradients

The dependence of structural parameters on the waveband carries information on the properties of stellar populations at different radii from the center of the galaxies. To investigate this subject, we derived the internal UV–OPT and OPT–NIR colour gradients for A 209, AC 118 and EIS 0048. We used the procedure described in LBM02: structural parameters were used to derive the colour  $\mu_2 - \mu_1$  of the galaxy at an inner radius  $r_i$  and at an outer radius  $r_o$ . Here, the symbols 1 and 2 denote the two wavebands. The colour gradient was obtained by the logarithmic gradient of  $\mu_2 - \mu_1$  (see Eq. (4) in LBM02). In order to make a direct comparison with previous works (PDI90, PVJ90), we adopted  $r_o = r_e$  and  $r_i = 0.1 \cdot r_e$ .

### 5.1. Distributions of colour gradients

Colour gradients for A 209, AC 118 and EIS 0048 are shown in Figs. 6–8, where upper and lower panels denote disks and spheroids. The bi-weight statistics was applied in order to characterize each distribution by the relative mean and standard deviation, whose values are summarized in Tables 4 and 5 for disks and spheroids, respectively. In the same tables, we also report the mean values of the UV–OPT and OPT–NIR central colours ( $\mu_2 - \mu_1$  at  $r = r_i$ ). The relative distributions and the standard deviations are not shown for brevity, since they are not relevant for the following analysis. The UV–OPT and OPT–NIR central colours will be used in Sect. 6 to discuss the origin of colour gradients. We note that the UV–OPT colour indicates  $B - R$  and  $V - I$  observed colours for A 209 and EIS 0048, respectively, while the OPT–NIR colour denotes  $R - K$  and  $I - K$  for AC 118 and EIS 0048, respectively. As mentioned in Sect. 2, the values of  $\text{grad}(\text{UV–OPT})$  and  $\text{grad}(\text{OPT–NIR})$  correspond approximately to  $\text{grad}(U - V)$  and  $\text{grad}(V - H)$  restframe, respectively.

#### 5.1.1. Disks

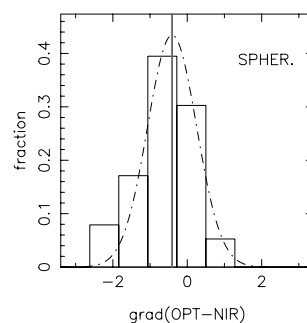
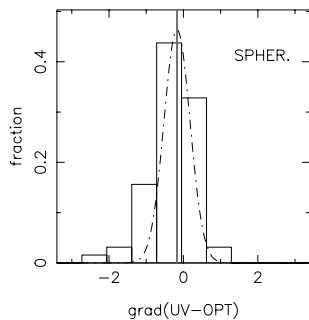
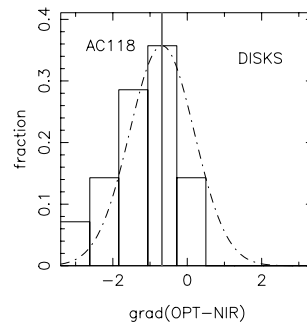
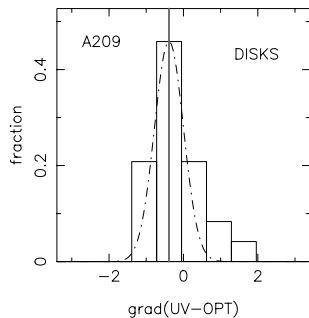
The mean value of the UV–OPT colour gradients (hereafter  $\text{grad}(\text{UV–OPT})$ ) amounts to  $\sim -0.4$  and is fully consistent

**Table 4.** UV–OPT and OPT–NIR colour gradients and central colours of disks.

$z$	grad (UV–OPT)		grad (OPT–NIR)		UV–OPT	OPT–NIR
	mean	std	mean	std	mean	mean
0.21	$-0.4 \pm 0.1$	$0.40 \pm 0.05$	...	...	$2.0 \pm 0.3$	...
0.31	...	...	$-0.68 \pm 0.12$	$0.87 \pm 0.30$	...	$3.80 \pm 0.13$
0.64	$-0.46 \pm 0.12$	$0.55 \pm 0.06$	$-1.2 \pm 0.1$	$0.5 \pm 0.3$	$2.2 \pm 0.4$	$4.0 \pm 0.4$

**Table 5.** UV–OPT and OPT–NIR colour gradients and central colours of spheroids.

$z$	grad (UV–OPT)		grad (OPT–NIR)		UV–OPT	OPT–NIR
	mean	std	mean	std	mean	mean
0.21	$-0.17 \pm 0.04$	$0.35 \pm 0.07$	...	...	$2.4 \pm 0.1$	...
0.31	...	...	$-0.40 \pm 0.14$	$0.6 \pm 0.1$	...	$3.8 \pm 0.2$
0.64	$-0.33 \pm 0.17$	$0.80 \pm 0.14$	$-0.38 \pm 0.15$	$0.56 \pm 0.15$	$2.6 \pm 0.2$	$3.6 \pm 0.2$

**Fig. 6.** Distribution of UV–OPT colour gradients for A 209. Upper and lower panels refer to disks and spheroids, respectively.**Fig. 7.** The same of Fig. 6 for the OPT–NIR colour gradients of galaxies in AC 118.

between A 209 and EIS 0048. This is due to the fact that the difference between OPT and UV structural parameters does not change significantly with redshift (Sect. 4.1). We note, however, that the distribution of EIS 0048 is more disperse and asymmetric with respect to that of A 209, with a significant fraction of galaxies ( $\sim 40\%$ ) having  $\text{grad}(\text{UV–OPT}) > 0$ . This is a consequence of what found in Sect. 4.1: some disks at  $z = 0.64$  have a light profile more peaked toward the center in the UV with respect to the optical, and show, therefore, positive values of  $\text{grad}(\text{UV–OPT})$ .

The most striking difference in OPT–NIR colour gradients ( $\text{grad}(\text{OPT–NIR})$ ) between AC 118 and EIS 0048 is the mean

value of the two distributions. As shown in Table 4, the mean value of  $\text{grad}(\text{OPT–NIR})$  is  $\sim -0.68$  at  $z = 0.31$  and  $\sim -1.2$  at  $z = 0.64$ , implying that there is a sharp evolution in the OPT–NIR colour gradients from  $z = 0.31$  to  $z = 0.64$ : the NIR light of disks become much more peaked in the center at higher redshift (cf. Sect. 4.1).

In order to account for field contamination<sup>4</sup> in the previous results, we proceeded as follows. As discussed in Sect. 2

<sup>4</sup> We point out that, since galaxies were selected by the photometric redshifts, field contaminants in the present sample are expected to lie approximately at the same redshift of cluster galaxies.

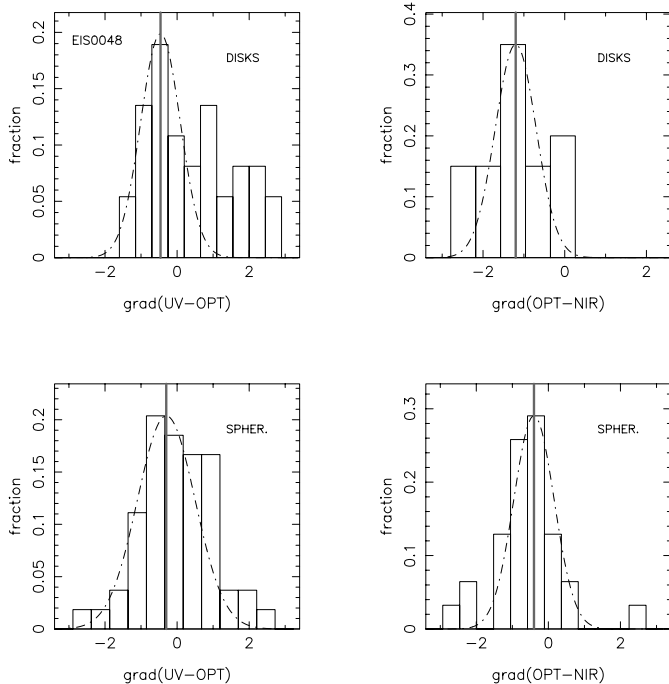


**Fig. 8.** The same of Fig. 6 for the UV–OPT and OPT–NIR colour gradients of galaxies in EIS 0048.

of Merluzzi et al. (2003), the effect of contaminants for AC 118 is expected to be negligible, while for EIS 0048 the fraction of field contaminants can be estimated as described in LMI03. By considering the colour distribution of disks at  $z = 0.64$ , we estimated that  $\sim 6$  (out of 20) galaxies in the OPT+NIR sample are expected to be field galaxies, and applied a statistically subtraction procedure to correct the distributions of colour gradients. The mean value of  $\text{grad}(\text{OPT-NIR})$  corrected for field contamination amounts to  $-1.35 \pm 0.07$ , which is in agreement with that given in Table 4. The same result holds for UV–OPT colour gradients.

### 5.1.2. Spheroids

By looking at Table 5, we see that the mean value of  $\text{grad}(\text{UV-OPT})$  is  $\sim -0.17$  at  $z = 0.21$  and  $\sim -0.33$  at  $z = 0.64$ . While this difference is not particularly significant ( $< 1\sigma$ ), the difference in the scatter of the two distributions is much more evident, as it is clearly seen by comparing Fig. 6 (lower panel) and Fig. 8 (lower – left panel). The standard deviation of  $\text{grad}(\text{UV-OPT})$  for EIS 0048 is more than double with respect to A 209. This is due to the fact that, as discussed in Sect. 4.2, the dispersions of the  $\Delta(\log r_e)$  and  $\Delta(\log n)$  distributions increase significantly from  $z = 0.21$  to  $z = 0.64$ .

The mean values of  $\text{grad}(\text{OPT-NIR})$  are  $\sim -0.51$  for AC 118 and  $\sim -0.38$  for EIS 0048, and are consistent within the relative uncertainties. We conclude, therefore, that no strong evolution in the OPT–NIR colour gradients is found between  $z = 0.31$  and  $z = 0.64$  for the population of spheroids.

**Table 6.** Parameters of colour gradient models of spheroids. Column 1: model. Columns 2, 3: inner and outer metallicities. Columns 4, 5: inner and outer ages. Notes: <sup>a</sup> constrained by both central colours and colour gradients, <sup>b</sup> the parameters are chosen in order to describe extremely negative colour gradients, <sup>c</sup> constrained by  $\text{grad}(\text{UV-OPT})$  at  $z = 0$ , <sup>d</sup> the parameters are chosen in order to describe positive colour gradients.

MOD	$Z_i$	$Z_o$	$T_i$	$T_o$
(1)	(2)	(3)	(4)	(5)
Z1	$3/2 Z_o^a$	$0.6 Z_i^a$	13 Gyr	13 Gyr
Z2 <sup>b</sup>	$3 Z_o$	$1/20 Z_i$	13 Gyr	13 Gyr
T1	$Z_o$	$Z_o$	13 Gyr	$0.62 T_i^c$
T2 <sup>d</sup>	$3 Z_o$	$3 Z_o$	$0.8 T_i$	13 Gyr
TZ	$3/2 Z_o^a$	$1/2 Z_o^a$	13 Gyr	$0.85 T_i^a$

## 6. Evolution of colour gradients

To investigate the origins of the observed gradients, we compare our results (colour gradients and central colours) with the predictions of population synthesis models.

### 6.1. Models

Colour gradients are modelled by using the GISEL00 synthesis code (Bruzual & Charlot 1993). Galaxies are described by an inner stellar population, with age<sup>5</sup>  $T_i$  and metallicity  $Z_i$ , and by an outer stellar population, with age  $T_o$  and metallicity  $Z_o$ . Each of them is characterized by an exponential star formation rate  $e^{-t/\tau}$ . For spheroids, we use  $\tau = 1$  Gyr, which gives a suitable description of the evolution of their integrated colours (e.g. Merluzzi et al. 2003), while for the disks we construct models with both  $\tau = 1$  Gyr and  $\tau = 3$  Gyr, in order to account for a star formation rate that lasts longer in time. For disks, we also consider the effect of dust absorption, by describing the inner and outer populations with colour excesses  $E(B - V)_i$  and  $E(B - V)_o$ , respectively. The absorption in UV–OPT and OPT–NIR colours is computed by using the extinction law from Seaton (1979). For A 209, AC 118 and EIS 0048, the colours of the inner and outer populations are obtained by using the instrumental response curves<sup>6</sup>, while colour gradients at  $z \sim 0$  are computed by using the  $U$ -,  $V$ -, and  $K$ -band filter curves from Buser (1978), Azusienis & Straizys (1969), and Bessell & Brett (1988), respectively.

Each gradient model is characterized by a set of parameters  $P_k(Z_i, T_i, \dots)$ , whose value is derived from the observations. To this aim, we minimize the chi-square:

$$\chi^2(P_k) = \sum [(E_k - O_k)^2 / \sigma_k^2], \quad (2)$$

where  $O_k$  and  $\sigma_k$  are the observed quantities (central colours and colour gradients) and the relative uncertainties at the different redshifts, while  $E_k$  are the model predictions for  $O_k$ .

<sup>5</sup> Here and in the following age refers to  $z = 0$ .

<sup>6</sup> The response curves were retrieved from the ESO Exposure Time Calculators at <http://www.eso.org/observing/etc/>

**Table 7.** Parameters of colour gradient models of disks. Column 1: model. Columns 2, 3: inner and outer metallicities. Columns 4, 5: inner and outer ages. Columns 6, 7: inner and outer colour excesses. Column 8: time scale of the star formation rate. Notes: <sup>a</sup> constrained by both central colours and grad(UV–OPT) at  $z = 0.21$  and  $z = 0.64$ , <sup>b</sup> constrained by the colour gradients, <sup>c</sup> constrained by both central colours and UV–OPT, OPT–NIR colour gradients, <sup>d</sup> the first value of  $E(B - V)_i$  refers to  $z = 0.21$  and  $z = 0.31$ , while the second one to  $z = 0.64$ .

MOD	$Z_i$	$Z_o$	$T_i$	$T_o$	$E(B - V)_i$	$E(B - V)_o$	$\tau$
(1)	(2)	(3)	(4)	(5)	(6)	(7)	(8)
Z1	$3Z_\odot^a$	$0.8Z_\odot^a$	13 Gyr	13 Gyr	0.	0.	1 Gyr
T1	$0.44Z_\odot^b$	$0.44Z_\odot^b$	13 Gyr	$0.55T_i^b$	0.	0.	1 Gyr
$\tilde{T}1$	$0.44Z_\odot^b$	$0.44Z_\odot^b$	13 Gyr	$0.55T_i^b$	0.	0.	3 Gyr
$\tilde{T}D$	$0.44Z_\odot^c$	$0.44Z_\odot^c$	13 Gyr	$0.55T_i^c$	$0.18^c$	$0.18^c$	3 Gyr
$D^d$	$Z_\odot$	$Z_\odot$	13 Gyr	13 Gyr	$0.15, 0.30^d$	0.	3 Gyr

### 6.1.1. Spheroids

We consider three kinds of gradient models: metallicity ( $Z$ ) models, age ( $T$ ) models, and metallicity+age ( $TZ$ ) models. The relevant information on the models are summarized in Table 6. For models ( $Z$ ), we assume that the inner and outer populations are coeval, with  $T_i = T_o = 13$  Gyr, while the values of  $Z_i$  and  $Z_o$  are changed. We consider two cases: model (Z1), whose inner and outer metallicities are constrained by the observations, and model (Z2), which describes a strong metallicity gradient, with  $Z_i = 3Z_\odot$  and  $Z_o = 1/20Z_i$ . We note that inverse metallicity models ( $Z_o > Z_i$ ) are not considered here since they are not consistent with the data (see Sect. 6.2). For models ( $T$ ), we assume that the inner and the outer stellar populations have the same metallicity,  $Z_i = Z_o$ , while  $T_o$  and  $T_i$  are changed. We consider two cases: model (T1) has  $T_i = 13$  Gyr,  $Z_i = Z_o$  and  $T_o < T_i$ , while model (T2) has  $Z_i = 3Z_\odot$ ,  $T_o = 13$  Gyr and a younger population in the inner region. The value of  $T_o$  for model (T1) is derived on the basis of the observations while for model (T2) we chose  $T_i = 0.8 \cdot T_o$ . We note that model (T2) describes a galaxy in which the stars redden toward the outskirts, and is considered in order to investigate the origin of positive colour gradients. Finally, in model (TZ) the inner population is old ( $T_i = 13$  Gyr), while  $Z_i$ ,  $Z_o$  and  $T_o$  are obtained from the observations.

### 6.1.2. Disks

The relevant information on the gradient models are summarized in Table 7. We consider the following models: metallicity ( $Z$ ) and age ( $T$ ) models, a “protracted” age ( $\tilde{T}1$ ) model, a protracted age+dust ( $\tilde{T}D$ ) model, and a “changing” dust ( $D$ ) model. For ( $Z$ ) and ( $T$ ) models, we consider only the models (Z1) and (T1) introduced for the spheroids, since (Z2) and (T2) are not relevant for the present discussion. Model ( $\tilde{T}1$ ) is similar to (T1) but is characterized by a more protracted star formation ( $\tau = 3$  Gyr) in both the inner and outer regions. The same value of  $\tau$  is used for models ( $\tilde{T}D$ ) and ( $D$ ). Model ( $\tilde{T}D$ ) differs from ( $\tilde{T}1$ ) for the presence of dust in the inner and outer regions. The values of  $E(B - V)_i$  and  $E(B - V)_o$  are assumed to be equal and are derived from the observations. Finally, model ( $D$ ) has  $Z_i = Z_o = Z_\odot$ ,  $T_i = T_o = 13$  Gyr,

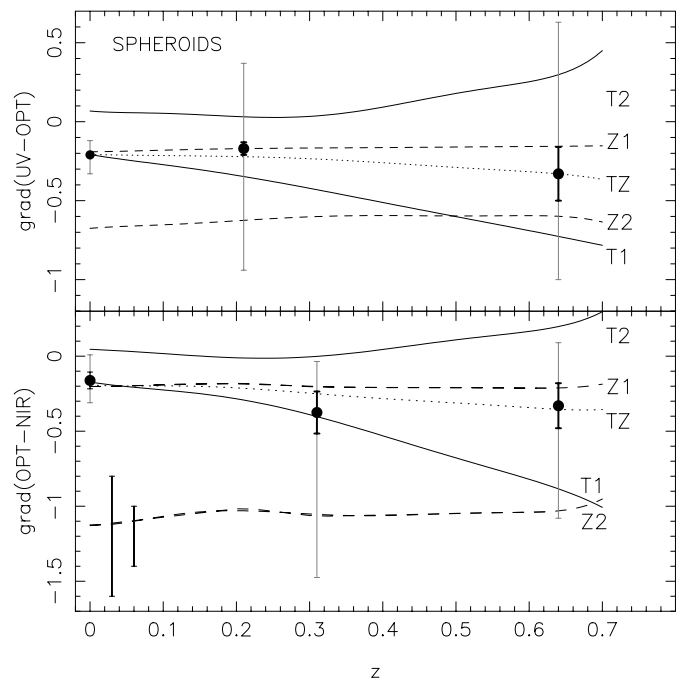


**Fig. 9.** UV–OPT and OPT–NIR colour gradients of spheroids as a function of redshift. The black and the grey error bars denote, respectively, the uncertainties on the mean value of the colour gradient and the 32% percentile interval of the distribution of colour gradients. Metallicity and age models are represented by the dashed and the continuous curves. The typical uncertainties on individual colour gradients are shown by the error bars in the lower-left of the bottom panel for AC 118 and EIS 0048 (left and right). Typical errors for A 209 are intermediate.

and  $E(B - V)_o = 0$ . The variation of colour gradients with redshift is described by changing the amount of dust absorption in the inner region between  $z \leq 0.31$  and  $z = 0.64$ .

## 6.2. Comparison with observations

The observed colour gradients are compared with the models in Figs. 9 and 10 for spheroids and disks, respectively. The curves in the figures were obtained by interpolating the values of the colour gradient models at  $z = 0, 0.21, 0.31$  and  $0.64$ .

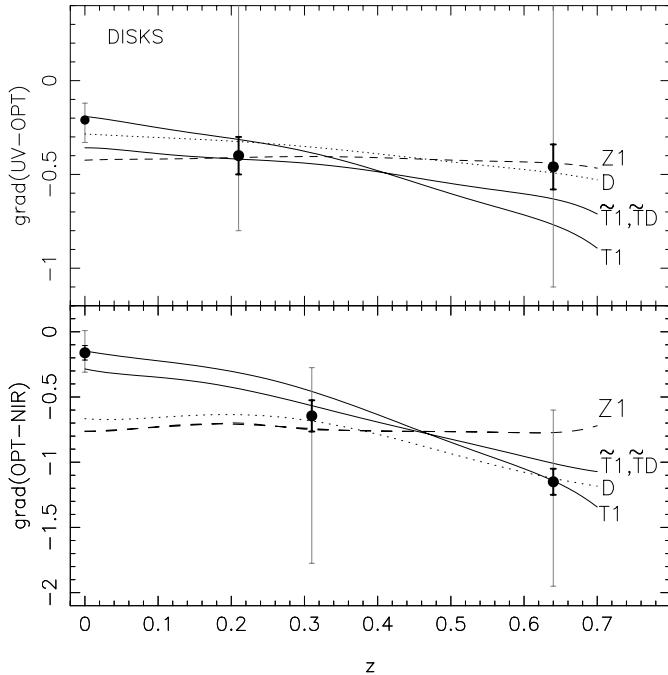


**Fig. 10.** Same of Fig. 9 for the disks.

To further constrain the models, we also considered measurements of colour gradients for nearby galaxies. For the spheroids, we use the UV–OPT values for a sample of 39 nearby ellipticals by PDI90, and the OPT–NIR colour gradients obtained by PVJ90 for 19 elliptical galaxies. For the disks, an homogeneous sample for which colour gradient measurements are available at  $z \sim 0$  both in UV–OPT and in OPT–NIR is not available, and therefore we consider, as reference, the values relative to the spheroids. In the figures, the black symbols denote the mean values of the colour gradients and the relative uncertainties ( $1\sigma$  standard intervals), while the grey bars, which mark the 32% percentile intervals of the gradient distributions, describe the range of values of colour gradients at each redshift.

The calibration of the models was performed by minimizing the “distance” (see Eq. (2)) of the model predictions from the observed quantities (central colours and/or colour gradients), as summarized in Tables 6 and 7.

### 6.2.1. Spheroids

By looking at Fig. 9, we begin to note that the size of the grey bars at  $z \sim 0$  are much smaller than those at higher redshift. Considering the typical uncertainty on the estimated colour gradients, we see that the difference is not due to the uncertainty on the estimate of structural parameters. The simplest explanation resides in the different selection criteria of our samples and those of PDI90 and PVJ90: the samples at  $z \sim 0$  consist, in fact, of morphologically selected elliptical galaxies, that, in many regards, are known to have very homogeneous properties (see e.g. van Dokkum et al. 1998). To discuss the

dispersion in the values of colour gradients, we will consider, therefore, only the estimates at  $z > 0$ .

Figure 9 shows that model Z1 gives a good description of all the observed colour gradients. Moreover this model produces the following central colours:  $(UV-OPT)_{0.21} \sim 2.65$ ,  $(UV-OPT)_{0.64} = 2.58$ ,  $(OPT-NIR)_{0.31} \sim 3.7$ ,  $(OPT-NIR)_{0.64} = 3.2$ . These values are consistent (within at most  $2\sigma$ ) with the observations (see Table 5). We also note that model Z1 produces very small OPT–OPT colour gradients in the considered redshift range (e.g.  $\text{grad}(R-I)_{0.31} = -0.04$ ), and is therefore in agreement with optical–optical estimates obtained by other studies for cluster galaxies at intermediate redshift (e.g. Saglia et al. 2000; Tamura & Ohta 2000). The age gradient model (T1) is consistent with the values of  $\text{grad}(OPT-NIR)$  at  $z \sim 0$  and at  $z \sim 0.31$ , as discussed in LBM02. However the other values of colour gradients exclude definitively this model, confirming that metallicity is the primary cause driving the colour gradients. For what concerns model TZ, we see that the combined effect of age and metallicity can explain to some extent both the colour gradients and the central colours at all redshifts. This model produces, in fact, the same central colours of model Z1 and is therefore in agreement with the values in Table 5. On the other hand, the very rapid decline of  $\text{grad}(UV-OPT)$  and  $\text{grad}(OPT-NIR)$  produced by age gradients (model T1) as a function of redshift, strongly constrain the maximum allowed age variation,  $\Delta(T)_{\max} = (T_i - T_o)_{\max}$ , from the galaxy center to the outskirts. In order to estimate  $\Delta(T)_{\max}$ , we shifted the values of the colour gradients and of the central colours according to the relative uncertainties and by using normal random deviates. For each iteration, we re-derived the values of  $Z_o$  and  $T_o$  of model (TZ). We found that the values of  $Z_o$  and  $T_o$  change according to the relation  $\delta(\log T_o) \sim -2/3\delta(\log Z_o)$ , which describes the well known age–metallicity degeneracy (Worthey et al. 1996), and that  $\sim 90\%$  of the  $T_o$  values are greater than  $\sim 10$  Gyr, constraining  $\Delta(T)$  to be smaller than  $\sim 23\%$  of  $T_i$ .

For what concerns the grey bars, we see that strong metallicity gradients (model Z2) are able to describe the tail toward negative values of the colour gradient distributions. The OPT–NIR diagram excludes, however, metallicity gradients stronger than that of model Z2, setting the constraint  $Z_o > 0.15 \cdot Z_o$ . Positive values of  $\text{grad}(UV-OPT)$  can be described by age models with  $T_i < T_o$ , like model T2. Inverse metallicity models ( $Z_i < Z_o$ ) give positive values of  $\text{grad}(UV-OPT)$  but too high values of  $\text{grad}(OPT-NIR)$ , and cannot fit, therefore, both gradients simultaneously. The OPT–NIR diagram excludes colour gradients significantly higher than those of model T2, setting the constraint  $T_i > 0.8 \cdot T_o$ .

### 6.2.2. Disks

By looking at Fig. 10, it is evident that metallicity models fail to reproduce the variation of  $\text{grad}(OPT-NIR)$  with redshift. Moreover, metallicity gradients in local disks are known to be small (e.g. Zaritsky et al. 1994) and therefore they cannot account for the large colour gradients observed in the present samples.

On the contrary, age models ( $T1$  and  $\tilde{T}1$ ) give a better description of the data. In model  $T1$ ,  $\text{grad}(\text{UV-OPT})$  varies too rapidly with redshift, deviating by  $\sim 3\sigma$  from the observed gradient at  $z = 0.64$ . Increasing the  $\tau$  value, the variation of  $\text{grad}(\text{UV-OPT})$  becomes milder, and the agreement improves<sup>7</sup>. Model  $\tilde{T}1$  is able, in fact, to reproduce within at most  $1.3\sigma$  the values of  $\text{grad}(\text{UV-OPT})$  and  $\text{grad}(\text{OPT-NIR})$  at any redshift, and gives colour gradients at  $z \sim 0$  which are only slightly bluer than those of the spheroids. Although age models reproduce the observed colour gradients, they fail to describe the red central colours of disks (Table 4), which are not significantly different from those of the spheroids (Table 5). Model  $\tilde{T}1$  gives  $(\text{UV-OPT})_{0.21} \sim 2.0$ ,  $(\text{UV-OPT})_{0.64} \sim 1.9$ ,  $(\text{OPT-NIR})_{0.31} \sim 3.0$ ,  $(\text{OPT-NIR})_{0.64} = 2.5$ , which are not consistent with the observations. We also note that, by increasing the inner and outer metallicities, the central colours are better reproduced, but the description of colour gradients worsens<sup>8</sup>. By fitting  $T_i$ ,  $T_o$ ,  $Z_i$ ,  $Z_o$  to both the colour gradients and the central colours, we found that these parameters are not able by themselves to describe all the observed quantities at better than  $2.5\sigma$ . We conclude, therefore, that stellar population parameters cannot explain alone our data.

The possible solution resides in dust absorption, which is known to produce strong colour gradients in nearby late-type spirals (Peletier et al. 1995). Model  $\tilde{T}D$  gives the same observed gradients of model  $\tilde{T}1$ , and produces the following central colours:  $(\text{UV-OPT})_{0.21} \sim 2.4$ ,  $(\text{UV-OPT})_{0.64} \sim 2.3$ ,  $(\text{OPT-NIR})_{0.31} \sim 3.9$ ,  $(\text{OPT-NIR})_{0.64} = 3.3$ , in good agreement ( $\leq 1.5\sigma$ ) with the values in Table 4. We point out that the present data can also be explained by models in which both age and dust content vary toward the periphery. In order to investigate this point, we considered  $T_o$  and  $E(B-V)_o$  in model  $\tilde{T}D$  as free parameters and fitted them to the observed quantities. The procedure was iterated by shifting the central colours and the colour gradients according to the corresponding uncertainties. We found that the change of  $T_o$  and  $E(B-V)_o$  are correlated, in the sense that  $\delta(\log T_o) \sim -1/3\delta(\log E(B-V)_o)$ , and that the variation of  $E(B-V)$  and  $T$  from the center to the periphery,  $\delta(E(B-V))$  and  $\delta(T)$ , are constrained in the ranges  $8\% \lesssim \delta(E(B-V)) \lesssim 17\%$  and  $45\% \lesssim \delta(T) \lesssim 48\%$  of the central values<sup>9</sup>. By increasing the inner and outer metallicities to  $Z_i = Z_o = 3/2 Z_\odot$ , the best fit values of  $E(B-V)_i$  is  $\sim 0.09$ , and the following constraints are obtained:  $30\% \lesssim \delta(E(B-V)) \lesssim 90\%$  and  $30\% \lesssim \delta(T) \lesssim 45\%$ . By increasing  $\tau$  to 10 Gyr (with  $Z_i = Z_o = 0.44 Z_\odot$ ), we obtain  $E(B-V)_i = 0.26$ ,  $51\% \lesssim \delta(E(B-V)) \lesssim 53\%$  and  $40\% \lesssim \delta(T) \lesssim 45\%$ . To summarize, in order to explain central colours and colour gradients of disks, both age gradients and dust absorption are needed. For a wide range of stellar

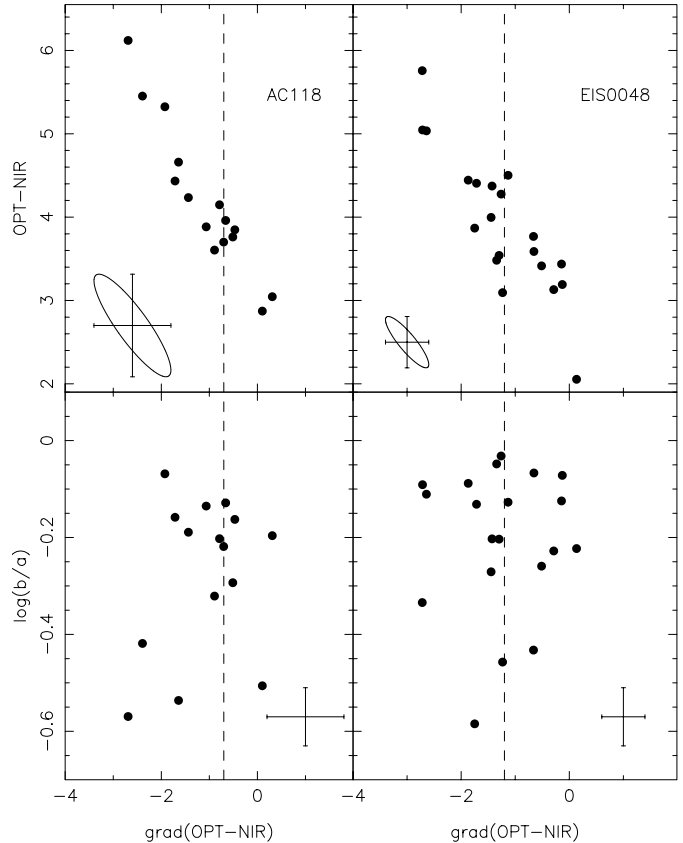


**Fig. 11.** OPT–NIR central colours and logarithm of axis ratio vs. OPT–NIR colour gradients for AC118 (left panels) and EIS0048 (right panels). Dashed lines mark the mean values of  $\text{grad}(\text{OPT-NIR})$ . The ellipses in the upper panels correspond to  $1\sigma$  confidence contours and show the correlation of the errors on OPT–NIR colours and colour gradients.

population parameters, the radial age variation is strongly constrained in the range  $[30, 50]\%$  of the central value, while  $E(B-V)_i$  is greater than  $\sim 0.1$ . On the other hand, the radial gradient of dust absorption depends critically on the inner metallicity and on the time scale of star formation rate.

So far, we considered only models for which the dust gradient does not change from one cluster to the other. By relaxing this assumption, the presence of age gradients is no more needed in order to explain all the observed quantities. This is shown by model  $D$ : a difference of the dust gradient between  $z \leq 0.31$  and  $z = 0.64$  also fits the data, giving central colours  $(\text{UV-OPT})_{0.21} \sim 2.4$ ,  $(\text{UV-OPT})_{0.64} \sim 2.5$ ,  $(\text{OPT-NIR})_{0.31} \sim 3.9$ ,  $(\text{OPT-NIR})_{0.64} = 3.8$ , which are in good agreement (at  $\leq 1.5\sigma$ ) with the values in Table 4. As shown by Peletier et al. 1995, useful tools to investigate the role of dust gradients in galaxies are the diagrams showing colour gradients against central colours and/or inclination. If dust is the primary effect driving the observed gradients (model  $D$ ), we would expect that redder and more inclined disks have also stronger OPT–NIR colour gradients for both AC118 and EIS0048. The diagrams are shown in Fig. 11. By analyzing the figure, it is important to take into account that the uncertainties on central colours and colour gradients are correlated. At least for AC118, this correlation fully explains the tight

<sup>7</sup> The UV–OPT colour is more sensitive with respect to OPT–NIR colours to the presence of young stars. For high values of  $\tau$ , the inner and outer stellar populations protract the formation of fresh stars with redshift, and therefore the evolution of  $\text{grad}(\text{UV-OPT})$  becomes smaller with respect to that of  $\text{grad}(\text{OPT-NIR})$ .

<sup>8</sup> In fact,  $\text{grad}(\text{UV-OPT})$  is more sensitive to the metallicity with respect to  $\text{grad}(\text{OPT-NIR})$ , in the sense that increasing  $Z_i$  and  $Z_o$ , the UV–OPT gradients decrease more rapidly than  $\text{grad}(\text{OPT-NIR})$ .

<sup>9</sup> The extrema mark a 10% percentile interval.

relation between grad (OPT–NIR) and the OPT–NIR colours, while for EIS 0048 some correlation could exist. On the other hand, the diagrams with inclination vs. grad (OPT–NIR) do not show any correlation at all (cf. Fig. 1 of Peletier et al. 1995). These facts seem to suggest that dust is not the primary cause of the observed gradients, and that models  $\tilde{T}D$  are a more suitable explanations of the present data.

Finally, some considerations are needed about the ranges of values of grad (UV–OPT) and grad (OPT–NIR). We see that age gradients stronger than  $T1$  can successfully describe the tails toward negative values of these distributions, with the constrain  $T_0 > 0.5 \cdot T_1$  set by grad (UV–OPT) at  $z = 0.64$ . For what concerns the positive values of grad (UV–OPT), which correspond to negative OPT–NIR gradients, they seem not to be explainable with the models considered above.

## 7. Summary and conclusions

We have studied the waveband dependence of the shape of the light distribution in cluster galaxies from  $z \sim 0.2$  to  $z \sim 0.64$ , by using a large wavelength baseline covering UV to NIR restframe. New structural parameters have been derived for the galaxy clusters A 209 at  $z = 0.21$ , in UV and OPT restframe ( $B$  and  $R$  bands), and for EIS 0048, at  $z = 0.64$ , in UV, OPT and NIR restframe ( $V$ ,  $I$  and  $K$  bands). Previous determinations of OPT and NIR ( $R$  and  $K$  bands) structural parameters for the cluster AC 118 at  $z = 0.31$  have also been used. The present data constitute the first large ( $N \sim 270$ ) sample of cluster galaxies with surface photometry from UV to NIR at intermediate redshifts. The analysis has been performed in terms of both structural parameters and colour gradients/central colours of galaxies, for the populations of disks and spheroids.

### 7.1. Spheroids

On average, the light profile of galaxies is more concentrated at longer wavelengths: effective radii decrease from UV to NIR, while Sersic indices increase. The values of  $\Delta(\log r_e)$  and  $\Delta(\log n)$  seem not to evolve significantly with redshift, although some differences (at  $\sim 2\sigma$ ) among the clusters could exist. By averaging the results for A 209, AC 118 and EIS 0048, we obtain  $r_e^{\text{UV}}/r_e^{\text{OPT}} = 1.2 \pm 0.05$ ,  $n^{\text{OPT}}/n^{\text{UV}} = 1.0 \pm 0.1$ , and  $r_e^{\text{OPT}}/r_e^{\text{NIR}} = 1.26 \pm 0.06$ ,  $n^{\text{OPT}}/n^{\text{NIR}} = 0.88 \pm 0.03$ . The value of  $r_e^{\text{OPT}}/r_e^{\text{NIR}}$  is fully consistent with that obtained for nearby early-type galaxies by Pahre et al. (1998), who found  $r_e^{\text{V}}/r_e^{\text{K}} \sim 1.2$ . The ratio of UV–OPT effective radii at  $z \sim 0$  can be estimated from the  $U$ - and  $R$ -band data of galaxies in rich nearby clusters by Jørgensen et al. (1995), and amounts to  $r_e^{\text{U}}/r_e^{\text{R}} \sim 1.17$ , which is in full agreement with our results. The bulk of spheroids shows negative colour gradients, both in UV–OPT and in OPT–NIR, and is therefore characterized by stellar populations redder in the center than in the periphery. The mean values of colour gradients are grad (UV–OPT) =  $-0.18 \pm 0.04$  and grad (OPT–NIR) =  $-0.4 \pm 0.1$ , and are consistent with the values obtained by PDI90, grad ( $U - R$ ) =  $-0.21 \pm 0.02$ , by Idiart et al. (2003), grad ( $U - V$ ) =  $-0.23 \pm 0.07$ , and by PVJ90, grad ( $V - K$ ) =  $-0.16 \pm 0.06$ , for nearby early-types. Moreover

the UV–OPT colour gradient is fully consistent with that estimated by Tamura & Ohta (2000) for cluster early-types at  $z \sim 0.4$ , grad ( $B_{450} - I_{814}$ ) =  $-0.23 \pm 0.05$ . We conclude, therefore, that the colour radial variation in spheroids does not change significantly at least out to  $z = 0.64$ . The comparison of colour gradients and central colours with gradient models of stellar population parameters shows that metallicity is the primary cause of the colour variation in galaxies, in agreement with previous optical studies at intermediate redshifts. The data are well fitted by models with super-solar inner metallicity ( $Z_i = 3/2 Z_\odot$ ), and with a pure metallicity gradient of about  $-0.2$  dex per decade of radius, in agreement with what found by Saglia et al. (2000) and Idiart et al. (2003). Taking into account age–metallicity degeneracies, however, mild age gradients are also consistent with our results, the age of stellar populations (referred to  $z = 0$ ) being constrained to vary by less than 25% from the center to the outskirts.

### 7.2. Disks

The light profiles of galaxies become more peaked in the center from UV to NIR. For what concerns structural parameters, we find that effective radii decrease at longer wavelengths, while Sersic indices become greater. The ratios of UV–OPT parameters and OPT–NIR effective radii do not show significant evolution with redshift. The mean values of  $r_e^{\text{UV}}/r_e^{\text{OPT}}$ ,  $n^{\text{UV}}/n^{\text{OPT}}$  and  $r_e^{\text{OPT}}/r_e^{\text{NIR}}$  amount to  $1.1 \pm 0.035$ ,  $0.84 \pm 0.03$  and  $1.25 \pm 0.04$ , respectively. The most sharp result, however, is the decrease in the ratio of OPT to NIR Sersic indices from  $z = 0.31$  to  $z = 0.64$ : the value of  $n^{\text{OPT}}/n^{\text{NIR}}$  varies from  $\sim 0.7$  at  $z = 0.31$  down to  $\sim 0.45$  at  $z = 0.64$ , implying that the OPT–NIR structure of disks becomes significantly more concentrated at higher redshift. When analyzed in terms of colour gradients, the previous results entail a presence of UV–OPT and OPT–NIR gradients much stronger with respect to those of spheroids. This is similar to what found in studies of colour gradients for nearby galaxies (e.g. Peletier et al. 1995). We find that the UV–OPT gradient does not vary significantly with redshift, and amounts to  $\sim -0.42$ , while, on the contrary, the value of grad (OPT–NIR) strongly decreases from  $\sim -0.7$  at  $z = 0.31$  down to  $\sim -1.2$  at  $z = 0.64$ . Moreover, disks have redder colours in the center, comparable to those of spheroids. We analyze these results by using simple gradient models describing the effect of variations of stellar population parameters as well as dust extinction throughout the galaxies. It turns out that two different kinds of models fit the present data.

1. Age gradient models with (i) a protracted star formation rate both in the inner and in the outer regions, and with (ii) a significant amount of dust extinction in the center. The property (i) keeps the variation of grad (UV–OPT) mild and allows the observed evolution of grad (OPT–NIR) to be reproduced, while the property (ii) is needed in order to describe the red central colours in disks. The better constrained quantities are the age gradient, in the range [30, 50]% of the central value, and the inner extinction,  $E(B - V)_i \gtrsim 0.1$ . On the other hand, the amount of dust in the outer region depends critically on the value of other

stellar population parameters (inner metallicity and time scale of star formation). It is interesting to note that the age gradient model predicts an UV–OPT colour gradient of  $\sim -0.35$  at  $z \sim 0$ , which is in very good agreement with that measured by Gadotti & dos Anjos (2001) for a sample of nearby late-type spirals,  $\text{grad}(\text{UV} - \text{OPT}) \sim -0.33$  (see their Table 2). The existence of age gradients in disk dominated galaxies is in agreement with what found by de Jong (1996) for nearby spirals, while the fact that dust absorption plays an important role in disks is in agreement with the findings of Peletier et al. (1995) for Sb and Sc galaxies at  $z \sim 0$ . Moreover, age gradients are a robust prediction of hierarchical models, in which disks are accreted by the condensation of gas from the surrounding halos.

2. Pure extinction models, in which the gradient of  $E(B - V)$  increases by a factor  $\sim 2$  for EIS 0048 with respect to the other clusters.

In order to discriminate between the two models, we analyze the relations between colour gradients and central colours/axis ratios. The present data indicate that galaxies with higher inclination do not have stronger colour gradients, as one would expect if dust gradients would be the main effect driving the observed gradients. Although some correlation between colour gradients and inclination could be hidden by the uncertainties on the above quantities, we argue that age gradient models could give a more suitable explanation of the present data.

Since hierarchical merging scenarios predict strong differences in the properties of field and cluster galaxies, it will be very interesting to analyze the role that environment has on the internal colour distribution of galaxies. Although we show by a statistical subtraction procedure that our results are not affected from field contamination, we cannot discriminate between the properties of field and cluster galaxies. In order to address this point, spectroscopic data will be needed.

*Acknowledgements.* We thank the ESO staff who effectively attended us during the observation run at FORS2. We thank M. Capaccioli and G. Chincarini for useful discussions. We are grateful to the referee, R. Peletier, for his comments, which helped us to improve the manuscript. Michele Massarotti is partly supported by a MIUR-COFIN grant.

## Appendix A: Reduction of FORS2 *I*-band images

New *I*-band images of the cluster of galaxies EIS 0048 have been collected at the ESO Very Large Telescope (VLT) during August 2001 with the FORS2 instrument, by using the high resolution observing mode (pixel scale  $0.1''/\text{pxl}$ ). The nights were photometric with excellent seeing conditions ( $0.3'' < FWHM < 0.4''$ ). The data consist of three pointings, for each of which we obtained five dithered exposures of 360 sec each. Data reduction was performed as described in LMI03, by using IRAF and Fortran routines developed by the authors. Images were bias subtracted and corrected for flat-field by using twilight sky exposures. The frames of each night were median combined in order to obtain a super-flat frame, that was used to improve the accuracy of the flat correction (at better than  $\sim 0.5\%$ ) and to fully remove the fringing pattern in the images (see LMI03 for details). The frames

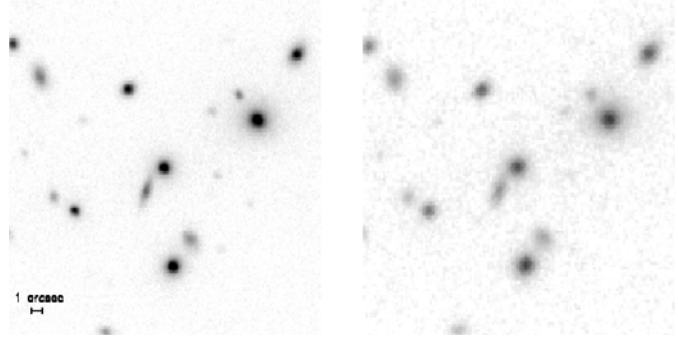


**Fig. A.1.** Image of the central region of EIS 0048 in the high resolution (left panel) and in the standard resolution (right panel) *I*-band images. The images are normalized to the same intensity scale. Note the spatial scale in the lower-left panel.

were registered by integer shifts and combined by using the IRAF task IMCOMBINE. The photometric calibration was performed into the Johnson-Kron-Cousins system by using comparison standard fields from Landolt (1992) observed during each night. The accuracy on the photometric calibration amounts to  $\sim 0.005$  mag. In Fig. A.1, we show, as example of the final quality of the image, the central region of the cluster. The image is compared with that obtained in the *I* band under more ordinary seeing conditions ( $FWHM \sim 0.8''$ ) with the standard resolution observing mode (pixel scale of  $0.2''/\text{pxl}$ , see LMI03).

## Appendix B: PSF of the FORS2 *I*-band images

The PSF of the FORS2 images was modelled by using a multi-Gaussian expansion, taking into account the effect of pixel convolution (see LBM02). Stars were selected according to the stellar index (SG) of SExtractor (Bertin & Arnout 1996). We considered only objects with  $I < 20$  and  $SG > 0.95$ , in order to obtain a reasonable accuracy in the fitting and to minimize the contamination by extended sources. In Fig. B.1, we show the contour plot for a star in the cluster field and the corresponding circular model, obtained as described in LBM02. It is evident that the star is asymmetric in a direction at  $\sim -45$  degrees with respect to the horizontal axis. This effect can be explained by the fact that five dithered exposures were available for each pointing and the seeing was not exactly the same for each of them. Since the images were combined by integer shifts, the seeing difference can easily account for the PSF asymmetry. We found that this effect can introduce a significant bias (10–15%) in the measurement of the structural parameters and, therefore, we considered more suitable models of the PSF, by using the rotation angle of each Gaussian as a free parameter in the fit and by introducing another free parameter to describe the deviations of the PSF isophotes from the circular shape. In Fig. B.1, we see that the asymmetric model matches very well the star isophotes. For each image, we fitted first each star separately, in order to investigate possible variations of the PSF across the chip, and then, since no significant dependence on the position was found, we constructed the PSF model by fitting all the stars simultaneously.

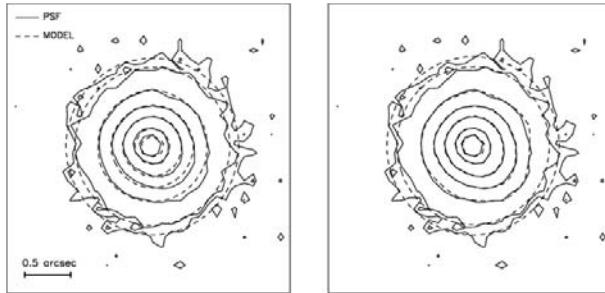


**Fig. B.1.** Modelling of the *I*-band PSF for EIS 0048. The contour plots refer to a star in the cluster field (continuous lines) and to the PSF models (dashed curves). Left and right panels show the symmetric and asymmetric models, respectively.

### Appendix C: Surface brightness profiles

The UV, OPT and NIR surface brightness profiles of the  $N = 273$  galaxies of A 209, AC 118 and EIS 0048 are shown in Figs. C.1–C.3<sup>10</sup>, respectively. The 1D profiles are plotted down to a signal to noise ratio  $S/N = 1$ . For each galaxy, we sampled the observed, fitted, and de-convolved images along ellipses with center coordinates, axis ratio, and position angle given by the two-dimensional fit, and derived the mean surface brightness  $\mu(r)$  as a function of the equivalent radius  $r$  of each ellipse. We considered only the pixels not masked in the 2D fit and excluded ellipses with a low fraction (<30%) of unmasked pixels. For the observed profiles, the error bars on  $\mu(r)$  were computed by taking into account the surface brightness fluctuations along the ellipses as well as the local background noise of each image. The profiles of galaxies belonging to multiple systems were obtained by first subtracting the 2D models of the companions from the observed galaxy image.

### References

- Abraham, R. G., Ellis, R. S., Fabian, A. C., Tanvir, N. R., & Glazebrook, K. 1999, *MNRAS*, 303, 641
- Andreon, S. 2001, *ApJ*, 547, 623, A01
- Azusienis, A., & Straizys, V. 1969, *Soviet Ast.*, 13, 316
- Beers, T. C., Flynn, K., & Gebhardt, K. 1990, *AJ*, 100, 32
- Bartholomew, L. J., Rose, J. A., Gaba, A. E., & Caldwell, N. 2001, *AJ*, 122, 2913
- Bertin, E., & Arnouts, S. 1996, *A&AS*, 117, 393
- Bessell, M. S., & Brett, J. M. 1988, *PASP*, 100, 1134
- Borson, T. A., Thompson, T. B., & Shectman, S. A. 1983, *AJ*, 88, 1707
- Bruzual, G. A., & Charlot, S. 1993, *ApJ*, 405, 538
- Busarello, G., Merluzzi, P., La Barbera, F., Massarotti, M., & Capaccioli, M. 2002, *A&A*, 389, 787, BML02
- Buser, R. 1978, *A&A*, 62, 411
- Caon, N., Capaccioli, M., & D’Onofrio, M. 1993, *MNRAS*, 265, 1013
- de Jong, R. S. 1996, *A&AS*, 118, 557
- Ebeling, H., Voges, W., Bohringer, H., et al. 1996, *MNRAS*, 283, 1103
- Franx, M., Illingworth, G., & Heckman, T. 1989, *AJ*, 98, 538
- Friaca, A. C. S., & Terlevich, R. J. 2001, *MNRAS*, 325, 335
- Gadotti, D. A., & dos Anjos, S. 2001, *AJ*, 122, 1298
- Hinkley, S., & Im, M. 2001, *ApJ*, 560, L41
- Idiart, T. P., Michard, R., & de Freitas Pacheco, J. A. 2003, *A&A*, 398, 949
- Jørgensen, I., Franx, M., & Kjærgaard, P. 1995, *MNRAS*, 273, 1097
- Kodama, T., & Arimoto, N. 1997, *A&A*, 320, 41
- La Barbera, F., Busarello, G., Merluzzi, P., Massarotti, M., & Capaccioli, M. 2002, *ApJ*, 571, 790, LBM02
- La Barbera, F., Merluzzi, P., Iovino, A., et al. 2003, *A&A*, 399, 899, LMI03
- Landolt, A. U. 1992, *AJ*, 104, 340
- Larson, R. B. 1974, *MNRAS*, 169, 229
- Lobo, C., Serote Roos, M., Durret, F., & Iovino, A. 2003, to appear in *Astrophysics and Space Sci. Ser.* (Kluwer Academic Publishers)
- Menanteau, F., Abraham, R. G., & Ellis, R. S. 2001, *MNRAS*, 322, 1
- Mercurio, A., Girardi, M., Boschin, W., Merluzzi, P., & Busarello, G. 2003a, *A&A*, 397, 431, MGB03
- Mercurio, A., Massarotti, M., Merluzzi, P., et al. 2003b, *A&A*, submitted, MMM03 [astro-ph/0303598]
- Merluzzi, P., La Barbera, F., Massarotti, M., Busarello, G., & Capaccioli, M. 2003, *ApJ*, accepted [astro-ph/0206403]
- Michard, R. 1999, *A&AS*, 137, 245
- Mihos, J. C., & Hernquist, L. 1994, *ApJ*, 427, 112
- Mihos, J. C., & Hernquist, L. 1996, *ApJ*, 464, 641
- Moriondo, G., Baffa, C., Casertano, S., et al. 2001, *A&A*, 370, 881
- Pahre, A. M., de Carvalho, R. R., & Djorgovski, S. G. 1998, *AJ*, 116, 1606
- Peletier, R. F., Davies, R. L., Illingworth, G. D., Davies, L. E., & Cawson, M. 1990a, *AJ*, 100, 1091, PDI90
- Peletier, R. F., Valentijn, E. A., & Jameson, R. F. 1990b, *A&A*, 233, 62, PVJ90
- Peletier, R. F., Valentijn, E. A., Moorwood, A. F. M., et al. 1995, *MNRAS*, 275, 874
- Ryder, S. D., & Dopita, M. A. 1994, *ApJ*, 430, 142
- Saglia, R. P., Maraston, C., Greggio, L., Bender, R., & Ziegler, B. 2000, *A&A*, 360, 911
- Seaton, M. J. 1979, *MNRAS*, 187, 73
- Silva, D. R., & Elston, R. 1994, *ApJ*, 428, 511
- Tamura, N., Kobayashi, C., Arimoto, N., Kodama, T., & Ohta, K. 2000, *MNRAS*, 119, 2134
- Tamura, N., & Ohta, K. 2000, *AJ*, 120, 533
- van Dokkum, P. G., Franx, M., Kelson, D. D., et al. 1998, *ApJ*, 500, 714
- White, S. D. M. 1980, *MNRAS*, 191, 1
- Wise, M. W., & Silva, D. R. 1996, *ApJ*, 461, 155
- Worthey, G., Trager, S. C., & Faber, S. M. 1996, in *Fresh Views of Elliptical Galaxies*, ed. A. Buzzoni, A. Renzini, & A. Serrano (San Francisco: ASP), ASP Conf. Ser., 86, 203
- Wu, X.-P., Xue, Y.-J., & Fang, L.-Z. 1999, *ApJ*, 524, 22
- Zaritsky, D., Kennicutt, R. C., Jr., & Huchra, J. P. 1994, *ApJ*, 420, 87

<sup>10</sup> Figures are fully available in electronic form at <http://www.edpsciences.org>

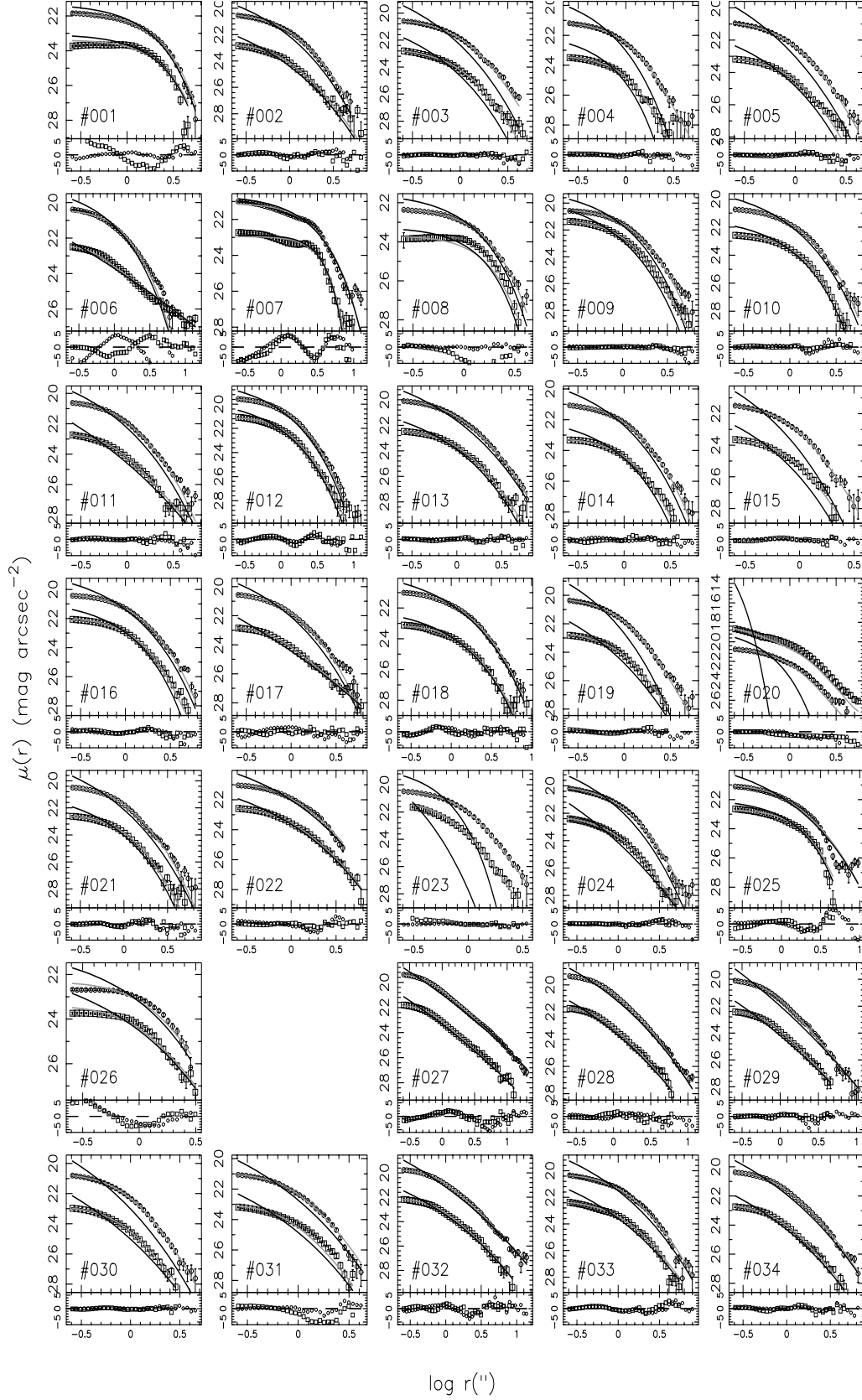


**Fig. C.1.** Surface brightness profiles,  $\mu(r)$ , of galaxies in A 209 are plotted versus the logarithm of the equivalent radius  $r$ .  $R$ - and  $B$ -band data are shown by circles and squares, respectively. For each band, fitted and de-convolved profiles are shown by grey and black curves, respectively. The residuals of the fits, in units of the error bars, are shown in the lower part of each panel. The pictures before and after the empty panel, are relative to disks and spheroids, respectively.

# Online Material

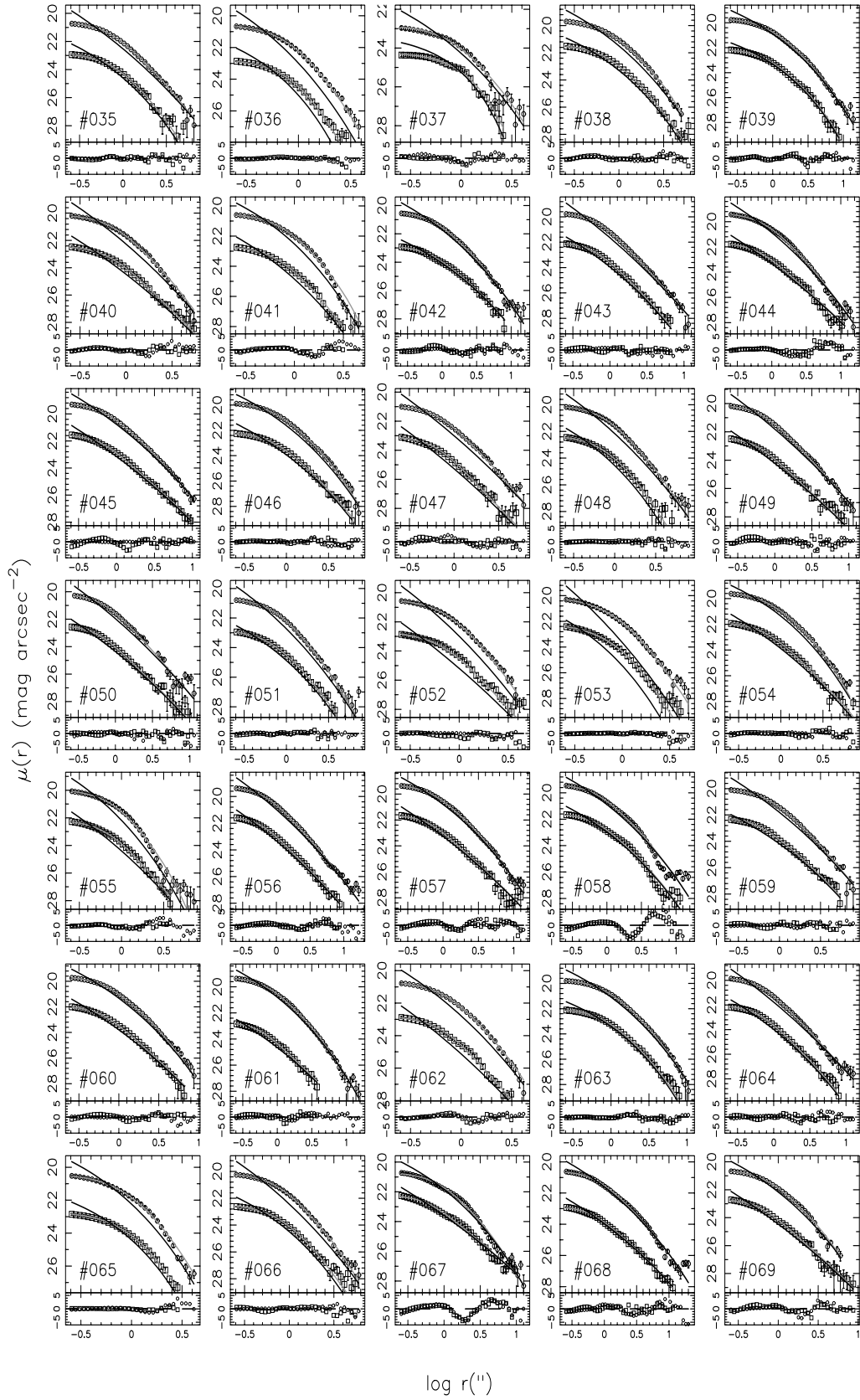


Fig. C.1. continued.

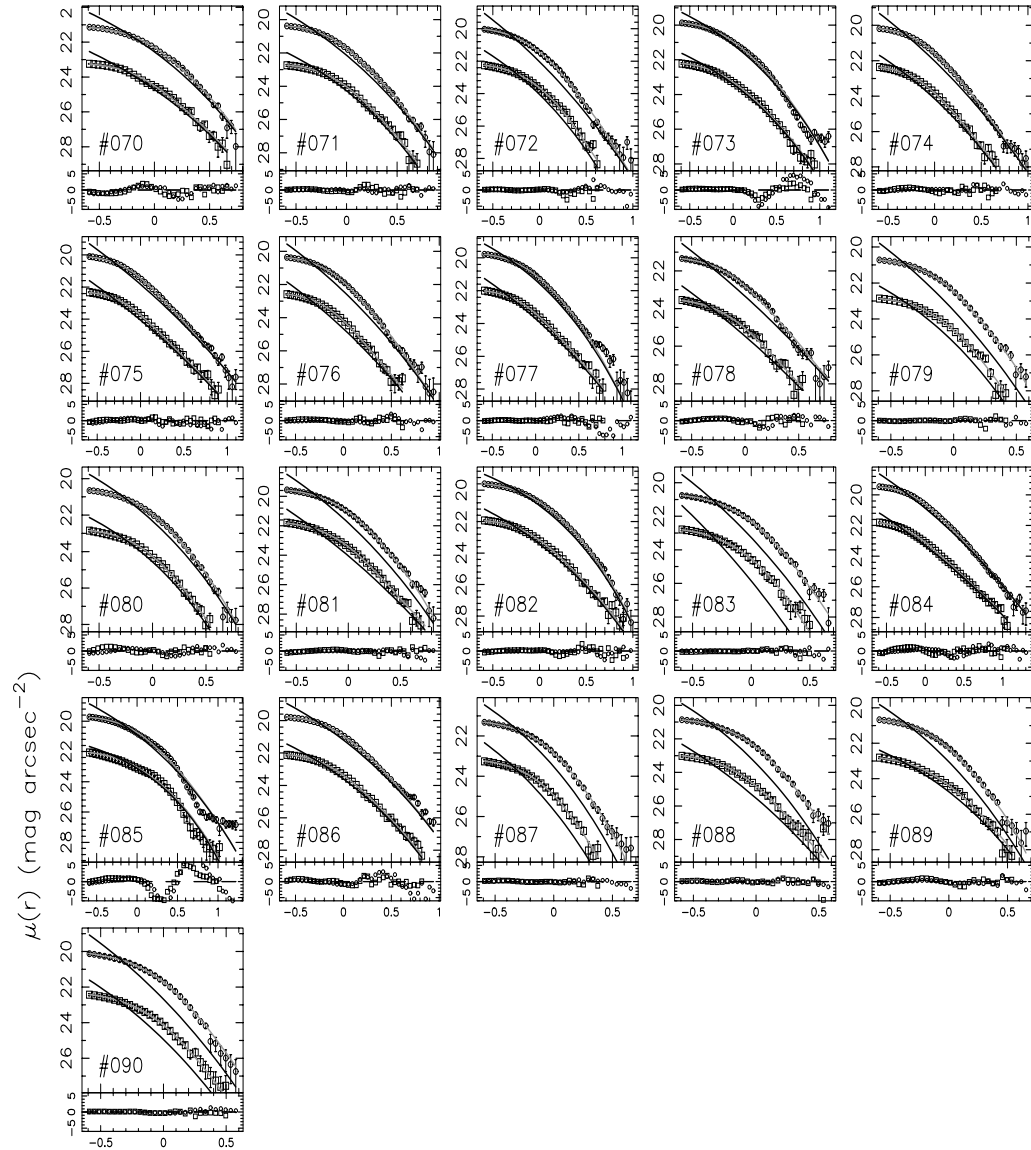
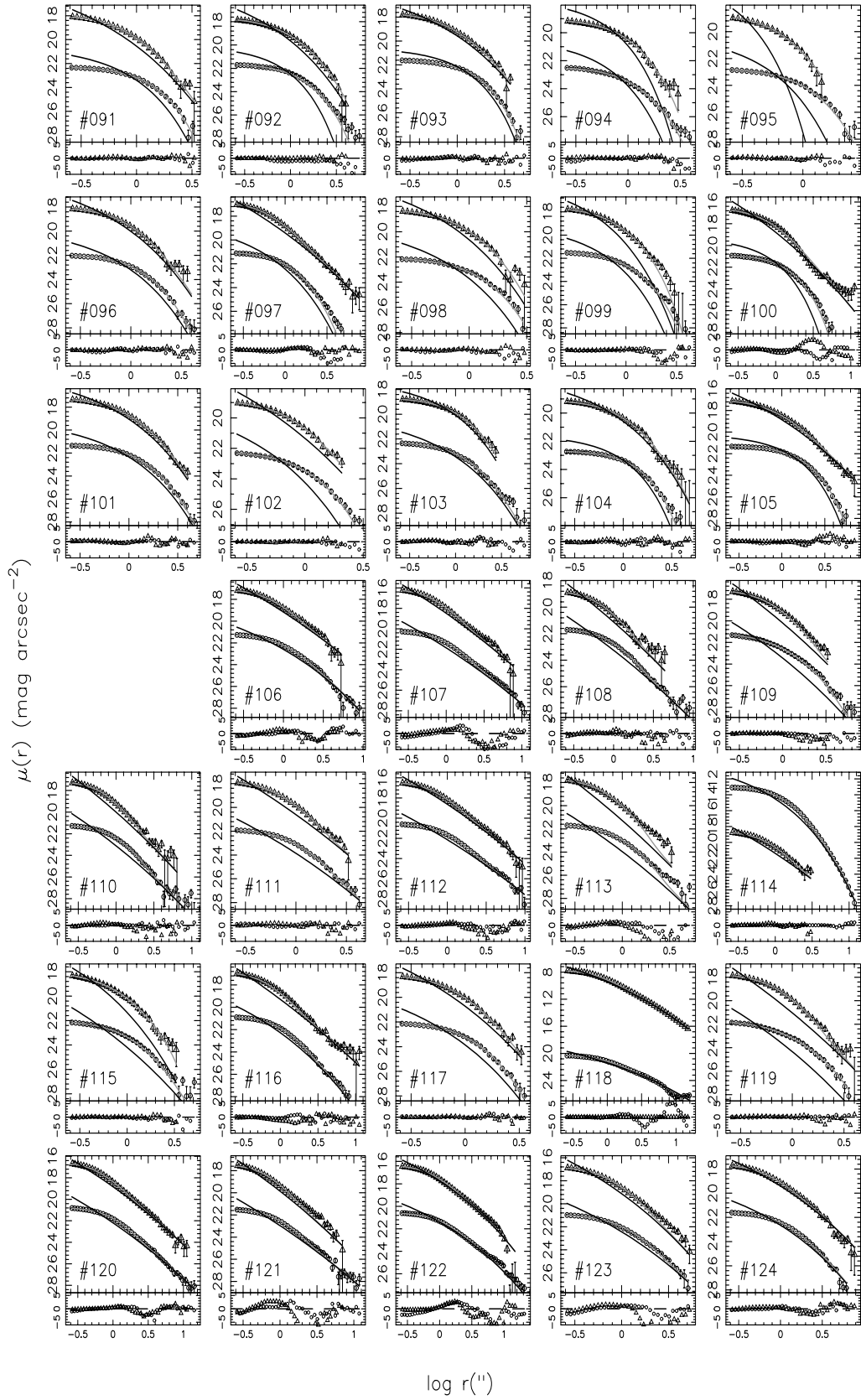


Fig. C.1. continued.



**Fig. C.2.** Same of Fig. C.1 for AC 118. *K*- and *R*-band data are shown by triangles and circles, respectively.

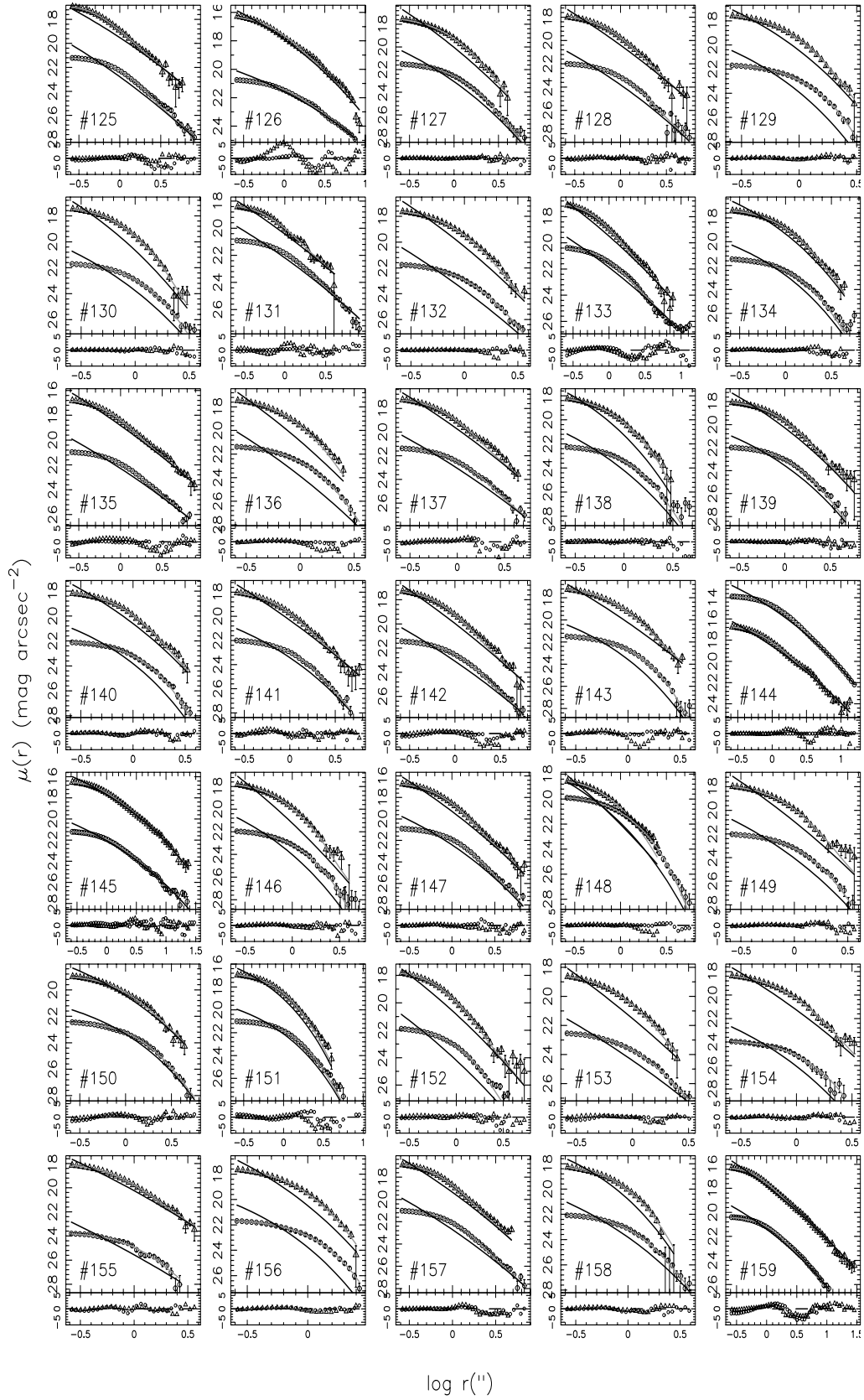


Fig. C.2. continued.

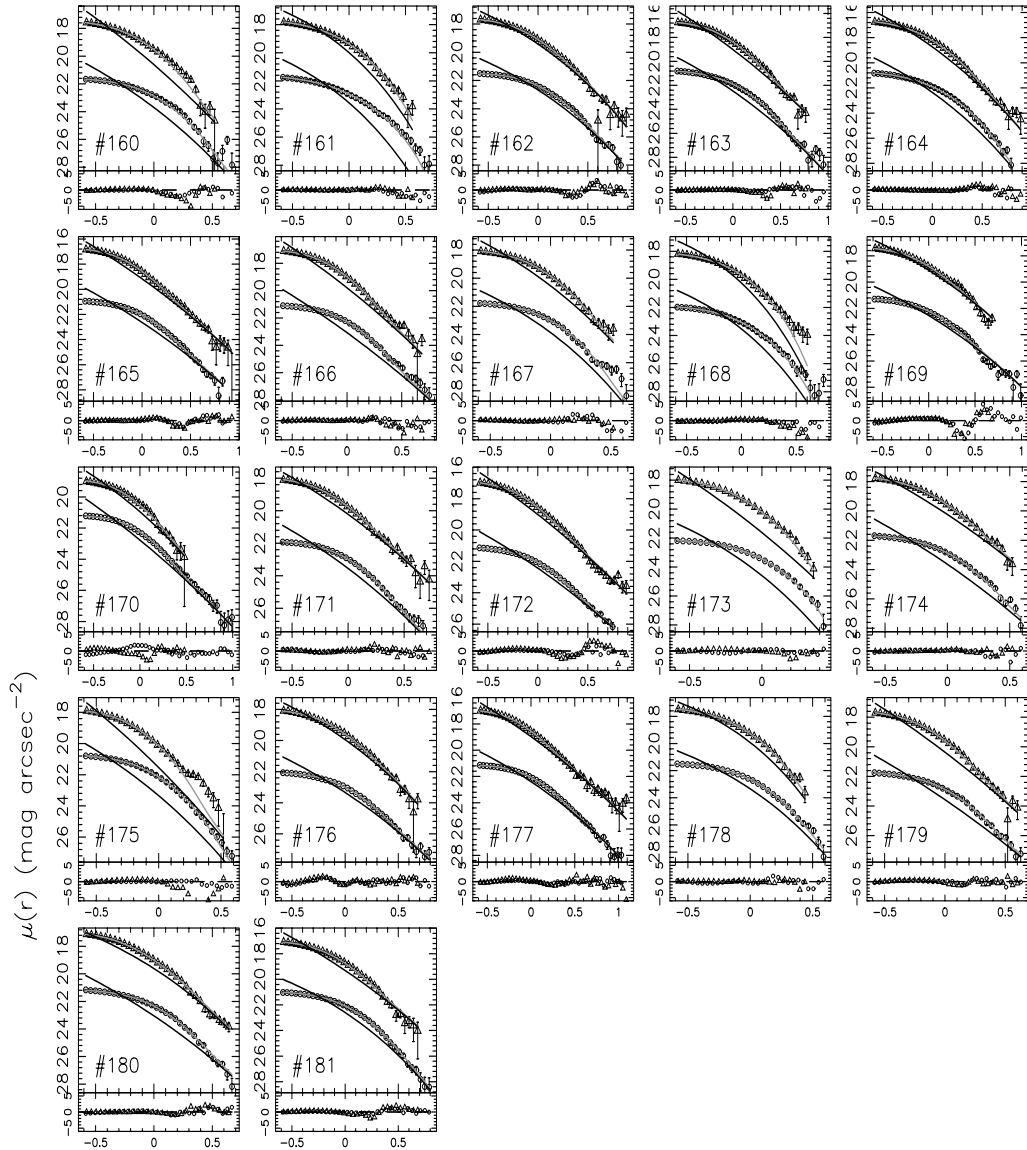
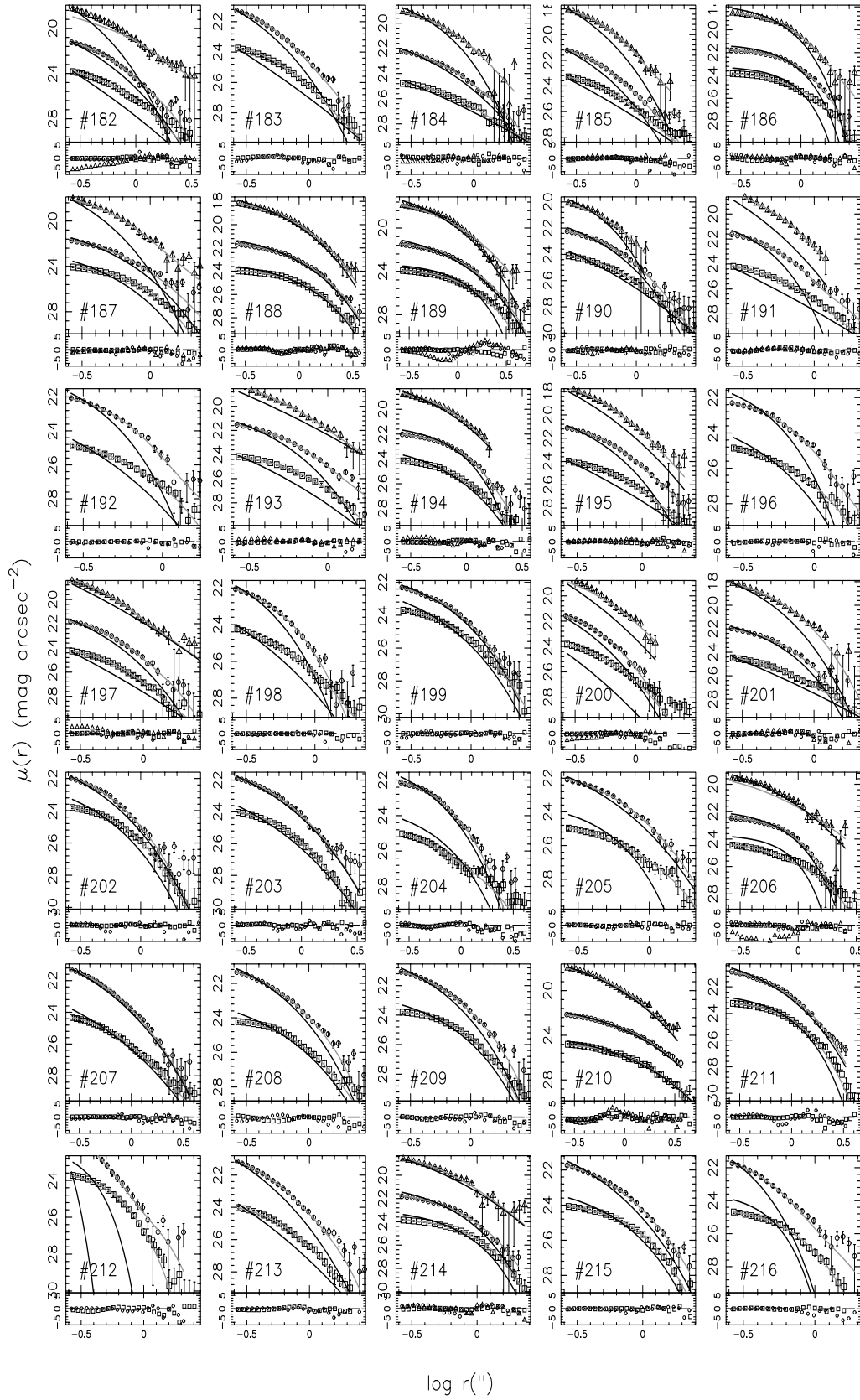


Fig. C.2. continued.



**Fig. C.3.** Same of Fig. C.2 for EIS 0048. UV, OPT and NIR data are shown by triangles, circles and squares, respectively. Note that one out of the  $N = 20$  disks with OPT and NIR data (gal. #199) does not have UV data, and therefore the total number of panels for the disks is 38.

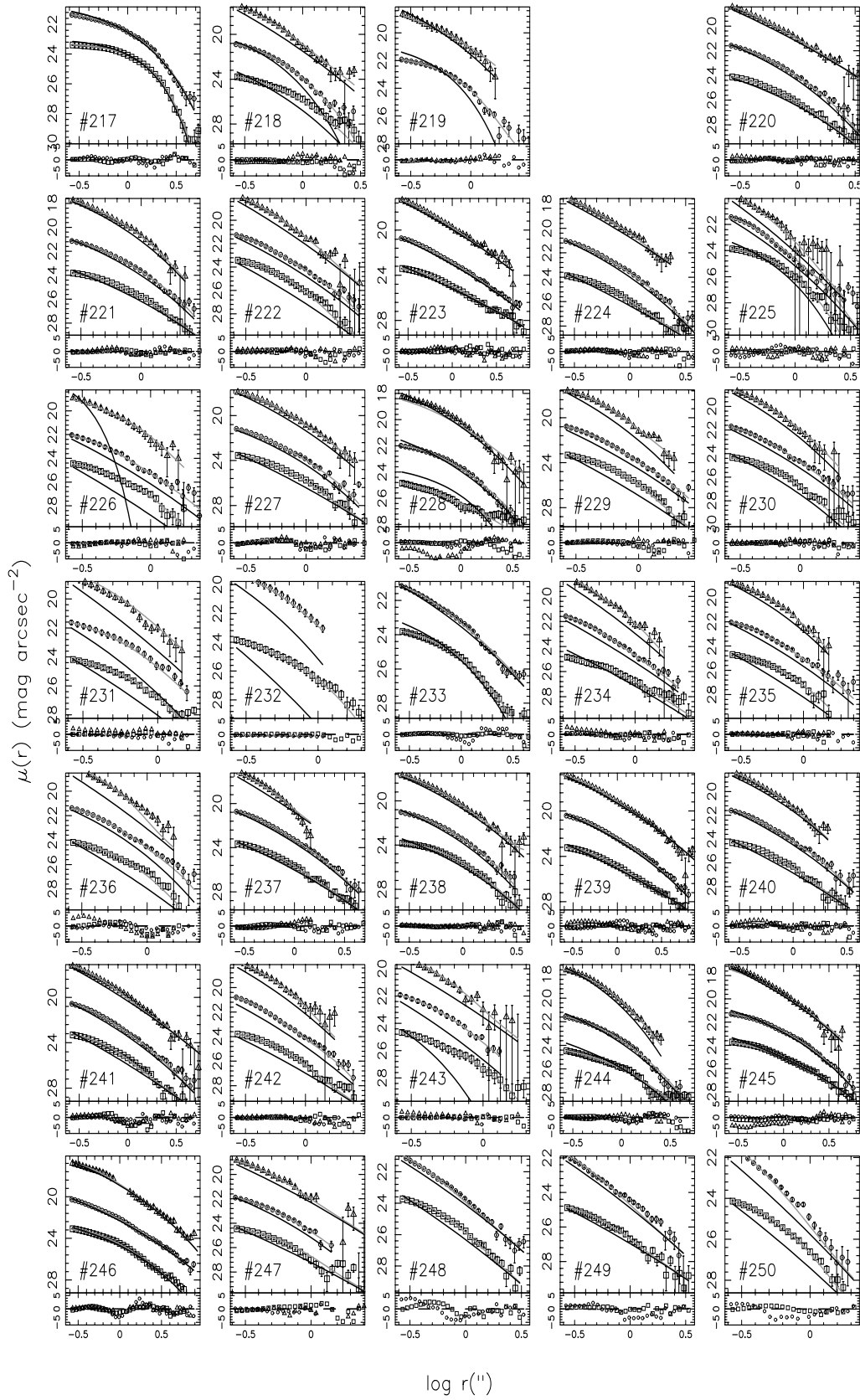


Fig. C.3. continued.

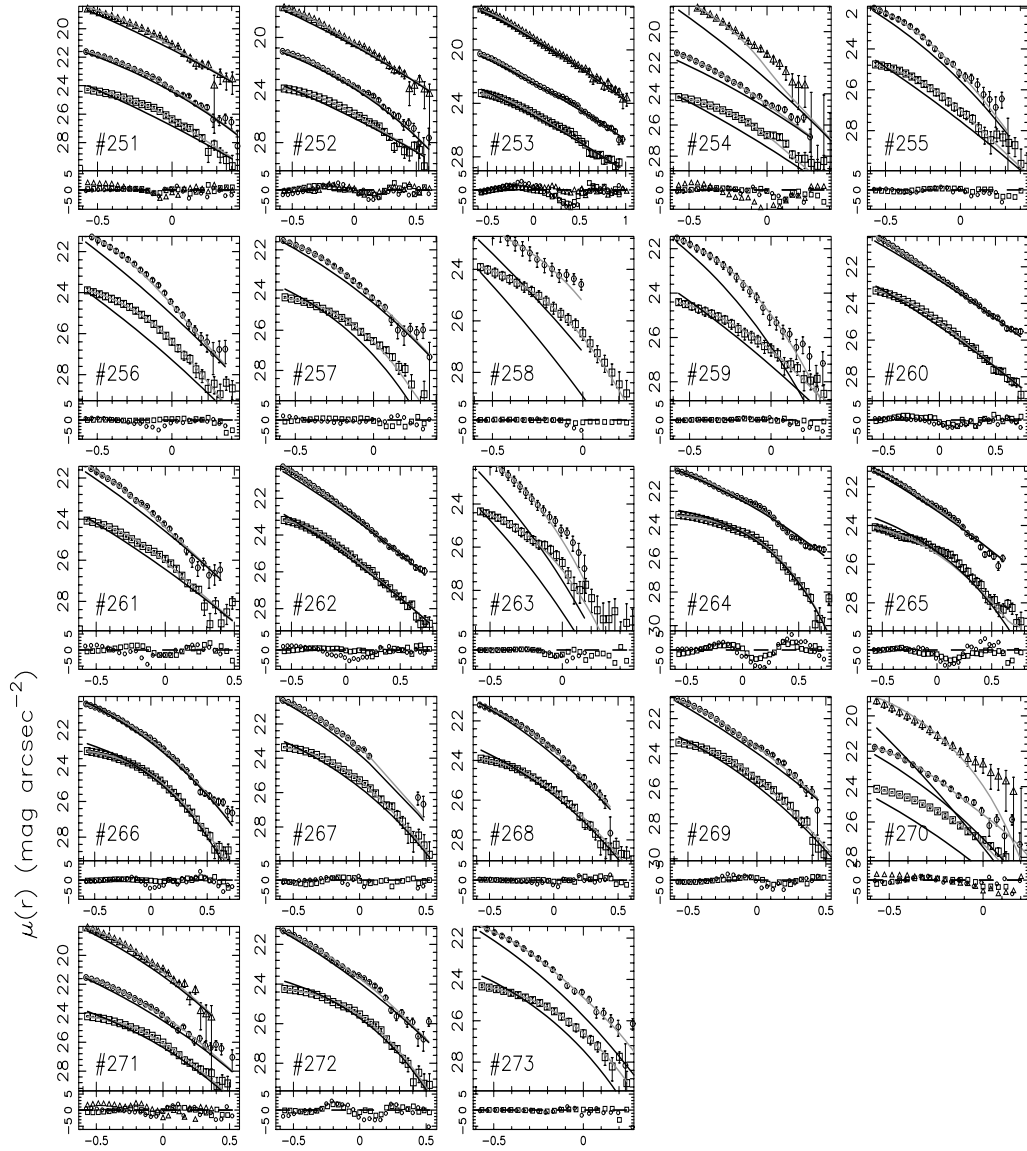


Fig. C.3. continued.